npj | quantum information

Article

Published in partnership with The University of New South Wales

https://doi.org/10.1038/s41534-026-01223-0

Improved strategies for fermionic quantum simulation with global interactions

Thierry N. Kaldenbach[1] ✉, Erik Schultheis[1], Niklas Stewen[2] & Gabriel Breuil[1]

We present efficient quantum circuits for fermionic excitation operators tailored for ion trap quantum computers exhibiting the Mølmer-Sørensen (MS) gate. Such operators commonly arise in the study of static and dynamic properties in electronic structure problems using Unitary Coupled Cluster theory or Trotterized time evolution. We detail how the global MS interaction naturally suits the non-local structure of fermionic excitation operators under the Jordan-Wigner mapping and simultaneously provides optimal parallelism in their circuit decompositions. Compared to previous schemes on ion traps, our approach reduces the number of MS gates by factors of 2-, and 4, for single-, and double excitations, respectively. These improvements promise significant speedups and error reductions, which we demonstrate by characterizing our circuits under a realistic pulse-level noise model of a linear ion trap quantum processor.

Among various expected use-cases of quantum computation, digital quantum simulation of fermionic many-body systems stands out as one of the most promising prospects[1–3]. Quantum simulations of electronic structure problems[4] are expected to yield unprecedented insight in fields ranging from quantum chemistry to materials science and engineering or drug discovery[5–8]. This expectation stems from the capability of quantum computers to exhibit superposition and entanglement, thus efficiently storing a combinatorially large number of electronic configurations, which is the bottleneck of many classical methods[1,2,4].

Electronic structure problems are typically mapped to quantum computers using a fermion-to-qubit mapping. In this formalism, the state of the system is encoded as a multi-qubit state and the Hamiltonian governing the problem is encoded as a weighted sum of Pauli operators. A large focus on fermionic mappings is dedicated to the optimization of mappings towards limited connectivity devices, where typically only interactions of one or two qubits are possible. One of the most popular approaches, the Jordan-Wigner (JW) transformation[9], is highly limited in its applicability on such devices due to its linear Pauli weight scaling. More sophisticated mappings can be used to tackle this obstacle, e.g., the Bravyi-Kitaev (BK) mapping[10,11] which achieves logarithmic localities. However, in practice, the benefit of logarithmic Pauli weight scaling is mitigated due to the need for many SWAP gates in the transpilation for a limited hardware connectivity[12]. Among numerous other approaches[13–17], tree-based mappings have recently proven to be particularly effective at simultaneously mitigating the Pauli weight and number of SWAP gates for specific connectivities[12,18].

The necessity for SWAP gates vanishes if one instead assumes a quantum device offering up-to-global interactions. Such interactions are provided on ion trap simulators[19,20] featuring the Mølmer-Sørensen (MS) gate[21,22], which can be used to efficiently implement non-local Pauli rotations arising under the chosen fermionic mapping. Most importantly, any Pauli rotation can be implemented using two MS gates regardless of the underlying locality[23]. In the context of fermionic systems, simulations leveraging the MS gate using the JW or BK mapping have been studied for dynamics in lattice models[24–26] and ground state computations in quantum chemistry[27–29] based on Unitary Coupled Cluster (UCC) theory[30–32].

The task of implementing arbitrary quantum circuits in terms of MS gates has been studied in Refs. 33,34. While ref. 34 already provides tight bounds on the number of MS gates for generic circuits, their algorithm gets outperformed by handcrafted results for specific unitaries[33,35,36]. The schemes presented in our work are specific to classes of unitaries in fermionic systems.

In this work, we show how the MS gate naturally implements the Pauli operator pool of fermionic and qubit excitation operators with maximum parallelism. Our approach exploits that specific types of MS gates perform simultaneous diagonalization of certain Pauli operators arising for excitation operators under the JW transformation. Using this feature, we leverage previous works, where each non-local Pauli operator is realized by its own pair of MS gates[23–25,28], and achieve an MS gate reduction by a factor of 2 for quadratic terms, and a factor of 4 for quartic terms. Our technique is also ancilla-free, making it not only faster, but also cheaper in terms of qubit requirements. By exploiting the local fermionic equivalences between (anti-)

[1]Institute of Materials Research, German Aerospace Center (DLR), Cologne, Germany. [2]Institute for Applied Physics, Technical University of Darmstadt, Darmstadt, Germany. ✉e-mail: thierry.kaldenbach@dlr.de

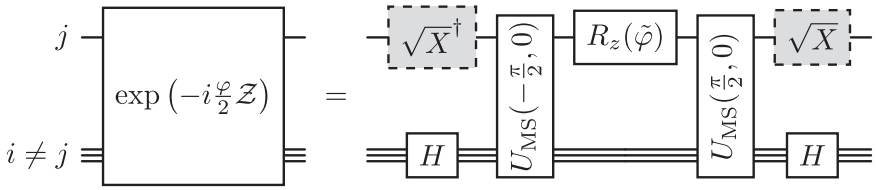

Fig. 1 | Circuit for digital quantum simulation with MS gates. Circuit decomposition of the global rotation $U(\varphi) = \exp(-i\varphi/2\mathcal{Z})$ using the **XX** gate. The rotation angle in the circuit is defined as $\tilde{\varphi} = (-1)^m\varphi$, where m follows the distinction between even qubit numbers $n = 2m$ and odd numbers $n = 2m + 1$ from equation (6). Gates with dashed lines are only required if n is even to turn Y_j into Z_j.

symmetrized excitation operators, we can use our circuits as building blocks for both UCC calculations, as well as the time evolution of electronic structure Hamiltonians in second quantization[37]. This enables the study of mixed quantum-classical dynamics within the Born-Oppenheimer approximation, thus providing an hybrid framework for studying time-dependent properties in molecules[6,37–39]. After introducing the fermionic building blocks, we explicitly outline our techniques at hand of the H_3^+ molecule by showing how UCCSD-, and time evolution circuits can be efficiently assembled. Finally, we demonstrate the efficiency of our circuit decompositions by characterizing the circuits via noisy simulations of molecular ground states of various molecules on an 12-qubit ion trap emulator at the pulse level.

Before presenting the results, we provide short introductions into general digital quantum simulations with MS gates, and the classes of fermionic operators used in UCCSD and Hamiltonian simulation. Readers with strong familiarity with those subjects are encouraged to skip to the results.

We first introduce the core properties of the MS gate and how to employ it to implement arbitrary Pauli rotations. For now, it is instructive to treat the MS gate as an idealized theoretical building block for quantum circuits, while an experimental description of the MS gate and its experimental challenges is later introduced in the results section. The MS gate captures all pairwise two-qubit interactions and is parametrized by the two parameters θ and ϕ,

$$U_{MS}(\theta,\phi) = \exp[-i\frac{\theta}{4}(\cos(\phi)S_x + \sin(\phi)S_y)^2]. \tag{1}$$

Here, θ is the phase and ϕ determines the type of interaction. The collective spin operators S_x and S_y are defined as the sum over all n qubits involved in the gate, e.g., $S_x = \sum_{i=1}^{n} X_i$. Through the course of this work, we are concerned with two special cases where the MS gate is a non-identity Clifford operation, namely the XX- and YY-type interactions:

$$\mathbf{XX} := U_{\mathrm{MS}}\left(\frac{\pi}{2}, 0\right) = \exp\left(-i\frac{\pi}{4}\sum_{j<k} X_jX_k\right), \tag{2}$$

$$\mathbf{Y\,Y} := U_{\mathrm{MS}}\left(\frac{\pi}{2}, \frac{\pi}{2}\right) = \exp\left(-i\frac{\pi}{4}\sum_{j<k} Y_jY_k\right). \tag{3}$$

The inverse gates $\mathbf{XX}^\dagger$ and $\mathbf{YY}^\dagger$ are obtained with $\theta = -\pi/2$, and due to the negative sign of θ sometimes referred to as "Backward" MS gates[23]. Experimentally speaking, sign changes of θ are inconvenient since they require frequency changes of the driving field[23]. This issue can be addressed by exploiting the local unitary equivalence between forward and backward MS gates, as detailed in the methods section. However, for the sake of a compact circuit notation, we use both the forward- and backward MS gates for our circuits in this work.

While the MS gate in equation (1) is globally defined, we typically do not want all qubits to interact at once. Instead, we need targeted MS gates acting on problem-specific subsets of qubits. From an experimental point of view, numerous approaches exist to restrict the MS interaction to subsets of the qubit array[23,40–43]. Alternatively, ions can be effectively decoupled by interspersing global MS gates with single-qubit gates[34,44]. Through this work, we make use of targeted MS gates, with the assumed experimental realization later outlined in the results section.

We now outline how any unitary Pauli rotation $U = \exp(-i\varphi/2\mathcal{P})$, where $\mathcal{P}$ is an N-qubit Pauli string $\mathcal{P} \in \{I, X, Y, Z\}^{\otimes N}$, is decomposed into a sequence of three gate operations up to local Clifford transformations – namely two MS gates and one local parameterized rotation. We mostly follow the same derivation as in ref. 23, however with an ancilla-free approach. For that purpose, we assume that $\mathcal{P}$ is n-local (with $n \leq N$) and, w.l.o.g. always acts non-trivially on some qubit j. Let us consider the unitary operator

$$U^{(j)}(\varphi) = \mathbf{XX}R_z^{(j)}(\varphi)\mathbf{XX}^\dagger, \tag{4}$$

where **XX** acts on all n qubits affected by the Pauli string $\mathcal{P}$, and $R_z^{(j)}(\varphi) = \exp(-i\varphi/2Z_j)$ is the single-qubit Z-rotation gate acting on qubit j. Since **XX** is Clifford, we may rewrite equation (4) as

$$U^{(j)}(\varphi) = \exp\left(-i\frac{\varphi}{2}\mathcal{P}^{(j)}\right), \tag{5}$$

where the generating Pauli string is given by $\mathcal{P}^{(j)} = \mathbf{XX}Z_j\mathbf{XX}^\dagger$. The structure of $\mathcal{P}^{(j)}$ is intrinsically linked to the locality n of the MS gate and the qubit j on which the R_z rotation is carried out,

$$\mathcal{P}^{(j)} = \mathcal{X}^{(j)} \otimes \begin{cases} (-1)^m Y_j, & \text{for } n = 2m, \\ (-1)^m Z_j, & \text{for } n = 2m+1, \end{cases} \tag{6}$$

where $\mathcal{X}^{(j)} = \otimes_{i\neq j} X_i$ and $m \in \mathbb{N}$. For the proof, refer to Supplementary Note 1. Any n-local Pauli string $\mathcal{P}$ either directly assumes the form in equation (6) through a suitable choice of j (n choices), or can be adjusted through local Clifford transformations accordingly. By instead using YY-type interactions in equation (4), one reverses the roles of X and Y in equation (6). This proves to be particularly convenient for the string pool in double excitations (cf. results).

In Fig. 1, we show how the **XX** gate is used in a quantum circuit to achieve an n-qubit Pauli-Z rotation, i.e., a rotation generated by $\mathcal{Z} = \otimes_{i=1}^{n} Z_i$. We compensate for the different cases in equation (6) by adjusting the rotation angle and/or adding local Cliffords based on the identity $\sqrt{X}Y\sqrt{X}^\dagger = Z$.

When instead decomposing an n-local Pauli rotation in terms of CNOT gates, a total number of $2(n-1)$ CNOTs is needed. Assuming full connectivity, these CNOTs could be arranged in $\mathcal{O}(\log(n))$ depth. In practice, however, this property can hardly be utilized due to the SWAP overhead. Meanwhile, the number of MS gates remains constant at 2. It should be emphasized that the MS gate time also grows with the with the number of interacting qubits. Hence, despite a constant gate count, the increase in locality is still not for free.

Having set the scene for arbitrary quantum simulations with MS gates, we now explore the class of fermionic operations subject to this work. The Unitary Coupled Cluster (UCC) ansatz is of particular interest due to its preservation of symmetries in electronic systems[45], such as the total particle

number or the spin. In its most general form, it is defined as

$$|\psi\rangle = \exp\left(\sum_N T_N\right)|\psi_0\rangle, \tag{7}$$

where $|\psi_0\rangle$ is an initial guess of the systems ground state – typically the Hartree-Fock ground state – and T_N denotes the N-th cluster operator incorporating all possible excitations of N electrons from occupied to virtual orbitals. In practice, N is often truncated at 2, giving rise to the UCCSD ansatz $\exp(i(T_1 + T_2))$, where the first- and second cluster operators

$$T_1 = \sum_{\substack{q \in \text{virt.} \\ p \in \text{occ.}}} \theta_p^q G_p^q, \text{ and } T_2 = \sum_{\substack{r,s \in \text{virt.} \\ p,q \in \text{occ.}}} \theta_{pq}^{rs} G_{pq}^{rs} \tag{8}$$

entail all possible generators of single- and double excitation generators, which are defined by the antisymmetrized terms

$$G_p^q = i(a_p^\dagger a_q - \text{H.c.}), \tag{9}$$

$$G_{pq}^{rs} = i(a_p^\dagger a_q^\dagger a_r a_s - \text{H.c.}), \tag{10}$$

respectively. Next, $\exp(T_1 + T_2)$ is typically approximated through a first-order Trotter-Suzuki product decomposition[46,47], such that the ansatz is a sequence of the single- and double excitation operators

$$U(\boldsymbol{\theta}) = \prod_{\substack{q \in \text{virt.} \\ p \in \text{occ.}}} U_p^q(\theta_p^q) \prod_{\substack{r,s \in \text{virt.} \\ p,q \in \text{occ.}}} U_{pq}^{rs}(\theta_{pq}^{rs}), \tag{11}$$

where

$$U_p^q(\theta) = \exp(-i\theta G_p^q), \tag{12}$$

$$U_{pq}^{rs}(\theta) = \exp(-i\theta G_{pq}^{rs}) \tag{13}$$

are the single- and double excitation operators, respectively. The challenge of UCC(SD) then lies in determining the parameters $\boldsymbol{\theta}$ to minimize the variational energy $E(\boldsymbol{\theta}) = \langle\psi_0|U^\dagger(\boldsymbol{\theta})HU(\boldsymbol{\theta})|\psi_0\rangle$. Cost-efficient updating schemes exploiting the spectral properties of excitations are detailed in refs. 48,49. Our work deals with the efficient circuit decomposition of excitations and is compatible with these parameter optimization schemes.

To study the non-adiabatic dynamics of quantum many-body systems, the time-dependent Schrödinger equation has to be solved. The solution is given by the time evolution operator, which is generated by the electronic structure Hamiltonian describing the fermionic many-body system. The time-dependent electronic structure Hamiltonian can be expressed in terms of the second-quantized operators and is defined as

$$H_{\text{el.}} = \sum_{pq} h_{pq} a_p^\dagger a_q + \frac{1}{2}\sum_{pqrs} h_{pqrs} a_p^\dagger a_q^\dagger a_r a_s, \tag{14}$$

where the one- and two-electron integrals h_{pq} and h_{pqrs} are subject to the permutational symmetries $h_{pq} = h_{qp}^*$ and $h_{pqrs} = h_{qpsr} = h_{rspq}^* = h_{srqp}^*$ [50]. More information on these integrals is provided in Supplementary Note 2. Here, we drop the explicit time dependence to shorten the notation. However, one could consider an explicit time dependence in the electron integrals due to dynamics in the nuclear coordinates. If one further assumes a time-dependent basis set, the fermionic operators would be time-dependent as well. We exploit these symmetries to rewrite the electronic Hamiltonian as $H_{el.} = H + \widetilde{H}$, with the antisymmetrized Hamiltonian H and symmetrized Hamiltonian $\widetilde{H}$

$$H = \frac{1}{2}\sum_{pq} \Im(h_{pq}) G_p^q + \frac{1}{4}\sum_{pqrs} \Im(h_{pqrs}) G_{pq}^{rs}, \tag{15}$$

$$\widetilde{H} = \frac{1}{2}\sum_{pq} \Re(h_{pq}) \widetilde{G}_p^q + \frac{1}{4}\sum_{pqrs} \Re(h_{pqrs}) \widetilde{G}_{pq}^{rs}, \tag{16}$$

where $\Re(\cdot)$ and $\Im(\cdot)$ denote the real- and imaginary parts, respectively. The symmetrized Hermitian generators $\widetilde{G}$ are given by

$$\widetilde{G}_p^q = a_p^\dagger a_q + \text{H.c.}, \tag{17}$$

$$\widetilde{G}_{pq}^{rs} = a_p^\dagger a_q^\dagger a_r a_s + \text{H.c.}, \tag{18}$$

while the antisymmetrized Hermitian generators G are the same as for the excitations in equations (9) and (10). For a detailed derivation, we refer the reader to Supplementary Note 3.

The time evolution of the electronic structure system is governed by the unitary time evolution operator $U(t, t_0) = \exp_{\mathcal{T}}(-i\int_{t_0}^t d\tau H_{el.}(\tau))$, where $\exp_{\mathcal{T}}$ denotes the time ordered operator exponential. For a small time step $\delta t = t - t_0$, we may approximate $U(t, t_0)$ through a first-order Trotter-Suzuki product formula

$$\begin{aligned} U(\delta t) \quad = \quad & \prod_{pq} U_p^q(\Im(h_{pq})\delta t) \prod_{pqrs} U_{pq}^{rs}(\Im(h_{pqrs})\delta t) \\ \times \quad & \prod_{pq} \widetilde{U}_p^q(\Re(h_{pq})\delta t) \prod_{pqrs} \widetilde{U}_{pq}^{rs}(\Re(h_{pqrs})\delta t), \end{aligned} \tag{19}$$

where U_p^q and U_{pq}^{rs} are the single- and double excitations from equations (12) and (13), and $\widetilde{U}_p^q$ and $\widetilde{U}_{pq}^{rs}$ are analogously defined with the symmetrized generators from equations (17) and (18). We want to highlight that the unitaries corresponding to the antisymmetrized Hamiltonian $\prod_{pq} U_p^q \prod_{pqrs} U_{pq}^{rs}$ are structurally similar to the UCCSD ansatz in equation (11), with the only differences being that no distinction between occupied and virtual orbitals is made and that shared indices (e.g., controlled excitations) are included.

Results

In this section, we first present our optimized circuits for antisymmetrized fermionic single- and double excitations. We then outline how our procedure generalizes to arbitrary excitation orders. We further discuss the applicability to other fermion-to-qubit mappings, and show how our techniques readily apply to qubit-excitations. We then show how the symmetrized fermionic terms for Hamiltonian simulation can be recovered from the previous circuits. We then give explicit circuit examples for UCCSD ansätze and Trotter steps. Last, we introduce a realistic pulse-level noise model, which we use to assess the practical improvements of our circuits in noisy scenarios.

Circuit for Single Excitations

Under the JW mapping (cf. methods), the generator of a single excitation between two orbitals p, q with $p < q$ assumes the Pauli decomposition

$$G_p^q \to \frac{1}{2}\mathcal{Z}_p^q(Y_p X_q - X_p Y_q), \tag{20}$$

with the parity string $\mathcal{Z}_p^q := \prod_{j\in\{p,q\}} \bigotimes_{k<j} Z_k$. We now reproduce equation (20) in terms of local operators and MS gates based on equation (6) to infer the circuit decomposition of $U_p^q(\theta)$. Since each Pauli string in the single excitation generator from equation (20) consists of one X and Y, the choice

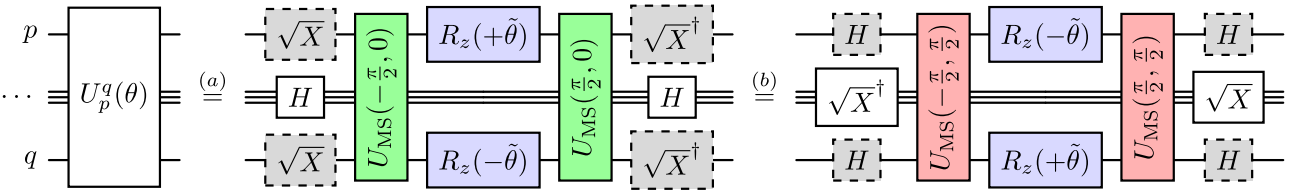

Fig. 2 | Circuit decompositions of the single-excitation gate. Circuit decomposition of the single-excitation gate $U_p^q(\theta) = \exp(-i\theta G_p^q)$ using (**a**) the **XX** gate and (**b**) the **YY** gate. The rotation angle in the circuits is defined as $\tilde{\theta} = (-1)^m\theta$, where m follows the same distinction between even qubit numbers $n = 2m$ and odd numbers $n = 2m + 1$ as before. Gates with dashed lines are only required if n is odd. The dots ⋯ labeling the quantum wire bundle represent all qubits affected by the parity string $\mathcal{Z}_p^q$.

of either the **XX** or **YY** gate is arbitrary. For the sake of simplicity, we only consider **XX** here.

We assume that the MS gate acts on all $n = q - p + 1$ qubits affected by the single excitation. The core idea is that we can realize up to n Pauli rotations in parallel by interspersing two MS gates with R_z gates. The generator of the single excitation entails two Pauli strings always acting at least on the two qubits p and q, therefore we use these two qubits to place the R_z gates in parallel.

For an even number of qubits $n = 2m$, we use

$$\mathbf{XX}(Z_p - Z_q)\mathbf{XX}^\dagger = (-1)^m\mathcal{X}_p^q(Y_pX_q - X_pY_q), \tag{21}$$

where $\mathcal{X}$ is analogously defined to $\mathcal{Z}$ with Pauli-X instead. Note that this is already local Clifford equivalent to equation (20) up to a Hadamard transformation on the qubits $p+1,\ldots,q-1$ and a prefactor of $(-1)^m/2$. For an odd number of qubits $n = 2m + 1$, we find

$$\mathbf{XX}(Z_p - Z_q)\mathbf{XX}^\dagger = (-1)^m\mathcal{X}_p^q(Z_pX_q - X_pZ_q). \tag{22}$$

Here, we obtain Z instead of Y. We circumvent that by exploiting that $\sqrt{X}^\dagger Z\sqrt{X} = Y$. By using this transformation on qubits p and q, we can change $Z \to Y$ without affecting X. Overall, this gives rise to

$$\begin{aligned}&\sqrt{X}_p^\dagger\sqrt{X}_q^\dagger\mathbf{XX}(Z_p - Z_q)\mathbf{XX}^\dagger\sqrt{X}_p\sqrt{X}_q\\ &= \mathbf{XX}(Y_p - Y_q)\mathbf{XX}^\dagger = (-1)^m\mathcal{X}_p^q(Y_pX_q - X_pY_q)\end{aligned} \tag{23}$$

The prefactor of $(-1)^m$ can in theory be absorbed into the variational parameter θ and thus be ignored in the circuit decomposition. However, we keep track of it as it becomes crucial for time evolution. Equations (21) and (23) give rise to the circuit decompositions of a single excitation with **XX** gates depicted in Fig. 2(a). An equivalent decomposition in terms of **YY** gates is provided in Fig. 2(b). In ref. 24, where every Pauli string is implemented with its own pair of MS gates, a total of 4 MS gates is required. With our parallelization, we achieve the same operation with only 2 MS gates, which is optimal with respect to the assumed gate set of targeted Clifford MS gates and arbitrary local unitaries.

Circuit for Double Excitations

The generator of the double excitation from modes p, q to r, s is decomposed as

$$\begin{aligned}&G_{pq}^{rs} \to \tfrac{1}{8}\mathcal{Z}_{pq}^{rs}\\ &\times(X_pY_qY_rY_s + Y_pX_qY_rY_s - Y_pY_qX_rY_s - Y_pY_qY_rX_s\\ &-Y_pX_qX_rX_s - X_pY_qX_rX_s + X_pX_qY_rX_s + X_pX_qX_rY_s),\end{aligned} \tag{24}$$

with the parity string $\mathcal{Z}_{pq}^{rs} := \prod_{j\in\{p,q,r,s\}}\bigotimes_{k<j}Z_k$. It involves two different sorts of Pauli strings, namely all permutations of $YXXX$ and $XYYY$ across the four orbitals p, q, r, s.

In the following, we assume that $p < q < r < s$, thus the MS gates act on the $n = (q - p) + (s - r) + 2$ qubits affected by the double excitation. In case that $q = p + 1$ and $s = r + 1$, the double excitation acts precisely on the 4 qubits p, q, r, s. These are the qubits we can generally use to deploy the R_z gates. Since the generator entails 8 strings, which we have to distribute among 4 qubits, we can not implement all strings at once. Instead, we need to distribute the rotations among two different layers, amounting to a minimum of 4 MS gates.

As introduced in the introduction, for an even number of qubits $n = 2m$, the $YXXX$-type strings can be readily realized in three layers using the **XX** gate:

$$\begin{aligned}&\mathbf{XX}(-Z_p - Z_q + Z_r + Z_s)\mathbf{XX}^\dagger = (-1)^m\mathcal{X}_{pq}^{rs}\\ &\times(-Y_pX_qX_rX_s - X_pY_qX_rX_s + X_pX_qY_rX_s + X_pX_qX_rY_s).\end{aligned} \tag{25}$$

For the $XYYY$-type strings, the same result can be achieved using **YY** interactions instead, thus circumventing the need for additional local transformations on the qubits p, q, r, s:

$$\begin{aligned}&\mathbf{Y}\,\mathbf{Y}(-Z_p - Z_q + Z_r + Z_s)\mathbf{Y}\,\mathbf{Y}^\dagger = (-1)^m\mathcal{Y}_{pq}^{rs}\\ &\times(X_pY_qY_rY_s + Y_pX_qY_rY_s - Y_pY_qX_rY_s - Y_pY_qY_rX_s).\end{aligned} \tag{26}$$

For an odd number of qubits $n = 2m + 1$, the results of equations (25) and (26) can be achieved similarly to equation (23) by employing the identities $X = HZH$ and $Y = \sqrt{X}^\dagger Z\sqrt{X}$. The resulting circuits can be inferred from Fig. 3. Compared to ref. 24, our technique reduces the number of MS gates from 16 down to 4, which is optimal.

If we relieve the constraint that excitations shall only occur from occupied to virtual orbitals, we can employ additional parallelizations. All distinct permutations of G_{pq}^{rs}, i.e., G_{pr}^{qs} and G_{ps}^{qr} give rise to the same eight Pauli strings, hence they can be implemented with the same cost as one double excitation by adjusting the angles in Fig. 3. We stress that this observation is not unique to our circuits and has already been efficiently employed in, e.g., ref. 51.

A double excitation where two indices are identical effectively boils down to a controlled single excitation

$$G_{pj}^{qj} = -ia_j^\dagger a_j(a_p^\dagger a_q - \mathrm{H.c}) = -n_jG_p^q, \tag{27}$$

where $n_j := a_j^\dagger a_j$ is the particle number operator, which makes j act as a control mode. While these types of excitations are typically neglected in UCCSD theory, they arise in generalized UCC theory, such as UCCGSD[52]. These terms further appear in the simulation of electronic structure Hamiltonians, which we will exploit later (cf. results). In addition, normal- and controlled single excitations are universal for particle-number preserving operations[53]. The controlled-singles circuits arise naturally from the regular singles circuits in Fig. 2 by replacing the $R_z(\theta)$ gates by controlled rotations. We leave the technical details to the methods section.

Circuit Costs for Higher Order Excitations

The expressivity of the UCCSD ansatz can be increased by including triple excitations (UCCSDT)[54] or even higher order terms[32]. The generator of an N-th order excitation generally assumes the form of 2^{2N-1} mutually commuting Pauli strings under the JW mapping, where each string consists of an

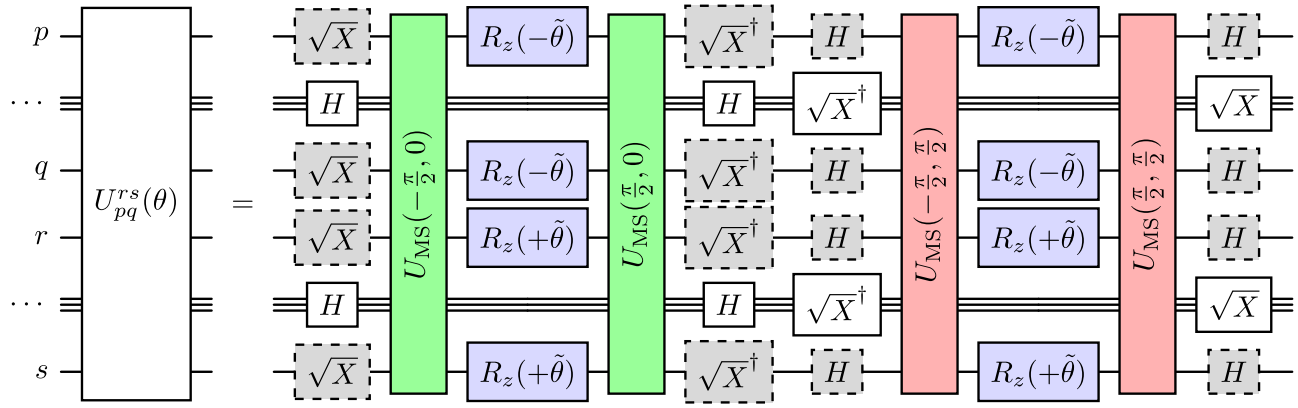

Fig. 3 | Circuit decomposition of the double-excitation gate. Circuit decomposition of the double-excitation gate $U_{pq}^{rs}(\theta) = \exp(-i\theta G_{pq}^{rs})$ using the **XX** and **YY** gates. The rotation angle in the circuits is defined as $\tilde{\theta} = (-1)^m\theta/4$, where m follows the same distinction between even qubit numbers $n = 2m$ and odd numbers $n = 2m + 1$ as before. Gates with dashed lines are only required if n is odd. The dots ⋯ labeling the quantum wire bundle represent all qubits affected by the parity string $\mathcal{Z}_{pq}^{rs}$.

odd number of X and Y operators[28]. Using the same parallelization strategy as for the singles and doubles, we can always implement subsets of N strings in parallel. Therefore, our approach reduces the MS count from 2^{2N} down to $2\lceil 2^{2N-2}/N\rceil$, thus providing an $\mathcal{O}(N)$ speedup.

We note that for any excitation order N, in principle, it is possible to capture the non-locality of the JW strings using only 2 global MS gates, at the start and end of the decomposition. The difference to our approach with multiple global MS gates then lies in the fact that the two MS gates are interspersed with all odd-parity (1, 3, …, $2N-1$) non-local Pauli-Z rotations, which are however local to the $2N$ qubits subject to the excitation. These could then in return again be decomposed in terms of smaller MS gates. However, the exponential cost is not removed, but rather relegated to the inner decomposition. More details on this mixed approach are provided in Supplementary Note 4.

Applicability to other Fermion-To-Qubit Mappings

We now shortly address if and how our parallelization techniques can be applied to other fermion-to-qubit mappings. For a simple illustration, we consider the generator of a single-excitation G_1^3 for a system with 4 fermionic modes, e.g., the H_2 molecule with a minimal active space of 2 electrons and four spin-orbitals, within the Parity[11] and the Bravyi-Kitaev (BK)[10] mappings. With the Parity mapping we obtain

$$G_1^3 = \frac{1}{2}(Z_0X_1Y_2 - Y_1X_2Z_3), \tag{28}$$

while the BK mapping yields

$$G_1^3 = \frac{1}{2}(Z_0Y_1Z_2 - Y_1Z_3). \tag{29}$$

The main insight is that for both mappings, a fermionic excitation potentially maps to Pauli strings acting on different subsets of qubits. In both examples, the two Pauli strings have different supports, and hence cannot be parallelized through means of equations (21) and (23). If one would like to implement the single excitation from equation (28) with MS gates using the decomposition technique from equation (6), one would need two MS gates for $Z_0X_1Y_2$ and another pair of MS gates for $Y_1X_2Z_3$. This results in more than the minimum amount of needed MS gates compared to JW. Since the Pauli strings in the parity mapping have the same $\mathcal{O}(N)$ locality scaling as in JW, we conclude that the parity mapping is less suitable for efficient simulations with global MS gates. Within the BK mapping, while the parallelization also fails, having more MS gates with only $\mathcal{O}(\log(N))$ locality might still prove beneficial, since the gates would be faster and less erroneous.

Applicability to Qubit Excitations

Qubit excitations have come up as a resource-friendly alternative to fermionic excitations for UCCSD theory[55]. In principle, qubit excitations differ from fermionic excitations in that they simply ignore the parity string in the generator, thus avoiding operations on the parity qubits of the excitations, and making the operation more resource-friendly. While this does not properly capture the fermionic character of the system, it works extremely well for variational problems such as UCCSD. We want to stress that all our circuits hold equivalently for qubit-excitations when removing the parity-qubits. Thus, our qubit single-excitations entails precisely two 2-qubit MS gates, and our qubit double-excitations consist of four 4-local MS gates. Our techniques are thus readily applicable to more hardware-friendly qubit excitation-based (QEB) notion of UCCSD.

Circuits for Hamiltonian Simulation

Concerning the symmetrized terms in the Hamiltonian from equation (16), we can trace them back to the antisymmetrized structure from UCCSD by exploiting the local equivalence of the antisymmetrized electron terms (single- and double- excitations) and the symmetrized electron terms in fermionic space:

$$\widetilde{G}_p^q = \exp(-i\frac{\pi}{2}n_p)G_p^q\exp(i\frac{\pi}{2}n_p), \tag{30}$$

$$\widetilde{G}_{pq}^{rs} = \exp(-i\frac{\pi}{2}n_p)G_{pq}^{rs}\exp(i\frac{\pi}{2}n_p). \tag{31}$$

Note that one could also use other particle number operators than n_p involved in the excitation (q for singles and q, r, s for doubles), but then for the orbitals in the superscript we have to replace $\pi/2 \to -\pi/2$. Also, for a controlled excitation G_{pj}^{qj}, only the modes p and q can be used. For more details, refer to Supplementary Note 5. Under the JW mapping, this local fermionic equivalence manifests as a local Clifford equivalence, i.e., $\exp(-i\pi/2n_p) \to S_p$ (up to a global phase which cancels out with the conjugate term), where S_p is the S-gate acting on qubit p. This way, we entirely avoid mapping out $\widetilde{G}$ with the JW mapping and instead can recycle the circuits from Figs. 2, 3, and 8. We point out that, unlike in variational applications, the phase $(-1)^m$ is important here to avoid accidentally performing backwards time evolution.

The only terms that can not be traced back to the excitation circuits are the density terms $\widetilde{G}_p^p$ and the Coulomb repulsion terms $\widetilde{G}_{pq}^{pq}$, which under the JW transformation map to

$$\widetilde{G}_p^p = 2n_p \to I - Z_p, \text{ and} \tag{32}$$

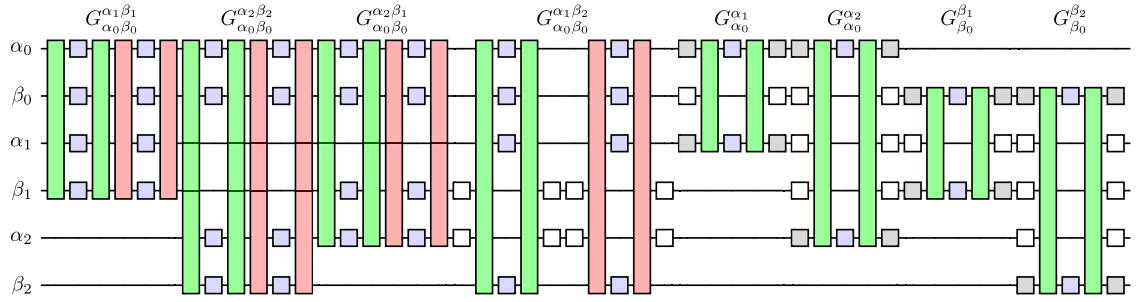

Fig. 4 | Schematic circuit decomposition of a UCCSD layer in first-order Trotterization. Schematic circuit decomposition of one layer of the UCCSD ansatz in first-order Trotterization. We use the same coloring scheme as for the previous figures; **XX** gates in green, **YY** gates in red, R_z gates in blue, local Cliffords in white if they are due to the parity string, gray if they account for odd numbers of qubits in the interaction. Note that some adjacent local Clifford gates cancel out and are only explicitly depicted for the sake of clarity.

$$\widetilde{G}^{pq}_{pq} = -2n_p n_q \to \frac{1}{2}(-I + Z_p + Z_q - Z_p Z_q). \tag{33}$$

These terms are at most 2-local, and the required R_{zz} gate for the ZZ terms can again be decomposed into MS gates as detailed in the introduction.

We supplement this section with the same remark as before - that all permutations of G^{rs}_{pq} give rise to the same string pool, and can thus be fully parallelized (the same holds separately for $\widetilde{G}$). Since for the two-electron integrals we generally have $h_{pqrs} \neq h_{prqs} \neq h_{psqr}$, the Pauli strings corresponding to G^{rs}_{pq}, G^{qs}_{pr} and G^{qr}_{ps} will in general not cancel out.

Finally, it is worth pointing out that real-valued orbitals effectively remove the antisymmetrized terms (equation (15)), thus cutting the number of non-local terms by half. In addition, more symmetries can be exploited, which however only reduce the R_z count and not the number of MS gates. We provide the technical details in the methods section.

Computational Goals of the Circuits

Our circuits are applicable to both time-dependent and time-independent studies. However, the time dependency brings an additional computational difficulty due to the coupling of electronic- and nuclear states. To tackle down this obstacle, techniques were developed leading to two types of quantum dynamics[56,57]. Either only the electronic motion is treated with quantum mechanics and the nuclear motion is evaluated classically, or both electronic and nuclear motions are treated with quantum mechanics. In the following, these two case are referred to as mixed classical-quantum dynamics, and fully-quantum dynamics, respectively.

The first type of dynamics, the mixed classical-quantum dynamic (MCQD) method, differs from molecular dynamics methods where the system is only treated classically and interatomic potentials are used to mimic interatomic interactions[58], whereas the electronic Schrödinger equation is not explicitly considered. For MCQD methods, the nuclei are also treated classically with Newton's equation of motion, and the Schrödinger equation is solved solely for the electrons[56]. Among the MCQD methods, either the dynamic is performed within a single electronic state, or the electronic wave-function evolves onto several electronic states and non-adiabatic couplings are involved in order to transfer the wave-function from one state to another. In any case, all electronic states in a MCQD method are determined within the Born-Oppenheimer approximation.

When only a single adiabatic electronic state (usually the ground-state) is considered, the electronic wavefunction is propagated onto this single potential energy surface, and all nuclei have a classical motions. This can be applied to describe atomic interactions in ground states[59], such as diffusion properties[60], reaction processes[61], and also the calculation of observables such as IR spectra[62]. One can use our UCCSD circuits to prepare a single adiabatic electronic state (usually the ground-state), and then slowly evolve it in a classical-quantum hybrid loop, where the UCCSD ansatz is used to update the electronic state based on the changed nuclear geometry.

When multiple adiabatic electronic states are considered[63], the electronic wavefunction can propagate among them through classical motion of the nuclei. This is formalized as the trotterized time evolution of a time-dependent electronic Hamiltonian, as detailed in ref. 39. Among the wide range of applications of such method, one can name photoisomerization processes[64], chemical processes in the atmosphere[65], and simulating the behavior of molecular aggregates for optoelectronics[66]. For such cases, one could start with UCCSD to prepare the ground state, and then non-adiabatically evolve it in time using the circuits for Trotterized Hamiltonian simulation.

The second type of dynamics entails a fully quantum mechanical treatment of both electrons and nuclei, and the Born-Oppenheimer approximation is not considered. These methods are very attractive for the time-study of quantum systems in the realm of non-adiabatic processes among several electronic states[67]. They are well known for studying internal conversion in conjugated chromophores (chemical processes involving bond breaking[68], carbon nanotube[69], non-radiative relaxation in chlorophylls[70]), energy transfer in molecular aggregates (dendrimers[71], or vibrational studies in OLEDs[72]). By encoding the vibrational modes of the nuclear motion into the normal modes of the ion chain of an ion trap computer[73], one could employ our time evolution circuits in a digital-analog fashion, as detailed in refs.[24,25]. A state-of-the-art implementation of such procedure is provided in refs. 74.

Example 1: A UCCSD Layer

We now provide some illustrative examples on how to assemble practical fermionic circuits within our gate decompositions.

Here, we demonstrate our technique on the $H_3{}^+$ molecule in the `STO-3G` basis set. This system entails 2 electrons distributed among 6 spin-orbitals, and thus provides a minimalist example with non-localities arising from the JW mapping in both the single- and double-excitations (or quadratic and quartic Hamiltonian terms). Note that we alternate the spin-up (α) and spin-down (β) orbitals in our state and operator notation, i.e., $|\alpha_0, \beta_0, \alpha_1, \beta_1, \alpha_2, \beta_2\rangle$. We use the same order to enumerate the orbitals in the JW mapping.

We start off by constructing the circuit for one first-order Trotter step in UCCSD theory. For that purpose, we are not concerned with the precise structure of the Hamiltonian, but rather the Hartree-Fock ground state $|\psi\rangle_{HF} = |110000\rangle$ and the eligible excitations starting from that state. Here, there are 4 unique spin-preserving single excitations $G^{\alpha_1}_{\alpha_0}$, $G^{\alpha_2}_{\alpha_0}$, $G^{\beta_1}_{\beta_0}$, and $G^{\beta_2}_{\beta_0}$. In addition, there exist 4 different spin-preserving double excitations $G^{\alpha_1,\beta_1}_{\alpha_0,\beta_0}$, $G^{\alpha_2,\beta_1}_{\alpha_0,\beta_0}$, $G^{\alpha_1,\beta_2}_{\alpha_0,\beta_0}$ and $G^{\alpha_2,\beta_2}_{\alpha_0,\beta_0}$. The quantum circuit corresponding to these excitations is schematically depicted in Fig. 4. Our circuit employs 24 MS gates while a string-by-string implementation amounts to 80 gates, hence we achieve a gate reduction by a factor of ~ 3.3.

Example 2: A Trotter Step of the Hamiltonian

We compute the one- and two-electron integrals with the `STO-3G` basis set in the equilibrium geometry, i.e., a bond distance of 0.784 Å and a bond

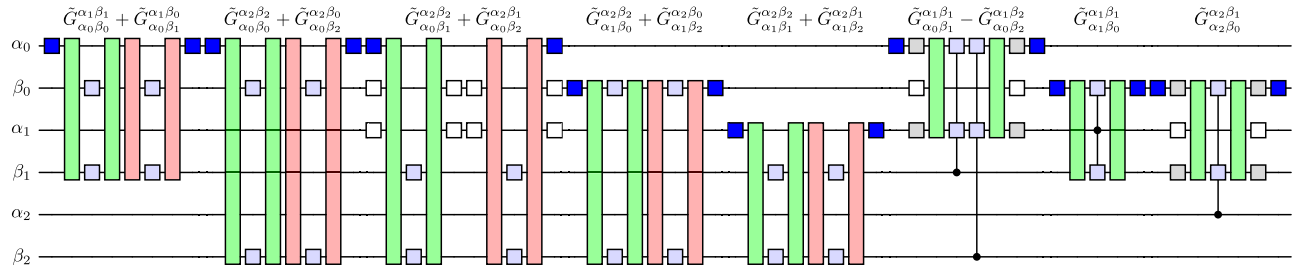

Fig. 5 | Schematic circuit decomposition of a Hamiltonian time step in first-order Trotterization. Schematic circuit decomposition of one Trotter step of $\exp(-i\delta t H_{non-loc.})$ in first-order Trotterization. We use the same coloring scheme as for the previous figures; **XX** gates in green, **YY** gates in red, R_z gates in blue, local Cliffords in white if they are due to the parity string, gray if they account for odd numbers of qubits in the interaction. In addition, we introduce dark blue gates representing the $S^{(\dagger)}$ gates ensuring the symmetrization. Note that some adjacent local Clifford gates cancel out and are only explicitly depicted for the sake of clarity.

angle of 60° using the `pyscf` package[75,76]. This gives rise to the Hamiltonian $H = H_{\text{loc.}} + H_{\text{non-loc.}}$ (we list the most significant terms in units of 1 Ha), where the local part containing terms of the type $\tilde{G}^{p}_{p}$ and $\tilde{G}^{pq}_{pq}$ is given by

$$\begin{aligned} H_{\text{loc.}} = &-0.917(\tilde{G}^{\alpha_0}_{\alpha_0}+\tilde{G}^{\beta_0}_{\beta_0}) \\ &-0.535(\tilde{G}^{\alpha_1}_{\alpha_1}+\tilde{G}^{\alpha_2}_{\alpha_2}+\tilde{G}^{\beta_1}_{\beta_1}+\tilde{G}^{\beta_2}_{\beta_2}) \\ &-0.337(\tilde{G}^{\alpha_1\beta_1}_{\alpha_1\beta_1}+\tilde{G}^{\alpha_2\beta_2}_{\alpha_2\beta_2})-0.307\tilde{G}^{\alpha_0\beta_0}_{\alpha_0\beta_0} \\ &-0.298(\tilde{G}^{\alpha_0\beta_2}_{\alpha_0\beta_2}+\tilde{G}^{\alpha_2\beta_0}_{\alpha_2\beta_0}+\tilde{G}^{\alpha_0\beta_1}_{\alpha_0\beta_1}+\tilde{G}^{\alpha_1\beta_0}_{\alpha_1\beta_0}) \\ &-0.265(\tilde{G}^{\alpha_1\beta_2}_{\alpha_1\beta_2}+\tilde{G}^{\alpha_2\beta_1}_{\alpha_2\beta_1}) \\ &-0.229(\tilde{G}^{\alpha_1\alpha_2}_{\alpha_1\alpha_2}+\tilde{G}^{\beta_1\beta_2}_{\beta_1\beta_2}) \\ &-0.226(\tilde{G}^{\alpha_0\alpha_1}_{\alpha_0\alpha_1}+\tilde{G}^{\alpha_0\alpha_2}_{\alpha_0\alpha_2}+\tilde{G}^{\beta_0\beta_1}_{\beta_0\beta_1}+\tilde{G}^{\beta_0\beta_2}_{\beta_0\beta_2}), \end{aligned} \tag{34}$$

while the non-local part reads

$$\begin{aligned} H_{\text{non-loc.}} = &-0.142(\tilde{G}^{\alpha_1\beta_1}_{\alpha_0\beta_0}+\tilde{G}^{\alpha_1\beta_0}_{\alpha_0\beta_1}+\tilde{G}^{\alpha_2\beta_2}_{\alpha_0\beta_0}+\tilde{G}^{\alpha_2\beta_0}_{\alpha_0\beta_2}) \\ &-0.090(\tilde{G}^{\alpha_1\beta_1}_{\alpha_0\beta_1}+\tilde{G}^{\alpha_1\beta_1}_{\alpha_1\beta_0}-\tilde{G}^{\alpha_1\beta_2}_{\alpha_0\beta_2}-\tilde{G}^{\alpha_2\beta_1}_{\alpha_2\beta_0}) \\ &+0.090(\tilde{G}^{\alpha_2\beta_2}_{\alpha_0\beta_1}+\tilde{G}^{\alpha_2\beta_1}_{\alpha_0\beta_2}+\tilde{G}^{\alpha_2\beta_2}_{\alpha_1\beta_0}+\tilde{G}^{\alpha_2\beta_0}_{\alpha_1\beta_2}) \\ &-0.072(\tilde{G}^{\alpha_2\beta_2}_{\alpha_1\beta_1}+\tilde{G}^{\alpha_2\beta_1}_{\alpha_1\beta_2}). \end{aligned} \tag{35}$$

Note that $\exp(-i\delta t H_{loc})$ trivially boils down to R_z and R_{zz} rotations according to equations (32) and (33). For that reason, we focus on the circuit decomposition concerning the non-local interactions.

Due to the symmetries for real basis sets, every term G^{rs}_{pq} with $p \neq q \neq r \neq s$ is accompanied by a term G^{rq}_{ps} which can be included without any additional MS gates. We can further exploit that the terms $\tilde{G}^{\alpha_1\beta_1}_{\alpha_0\beta_1}$ and $\tilde{G}^{\alpha_1\beta_2}_{\alpha_0\beta_2}$ correspond to the same excitation controlled by different modes, and can thus be parallelized as well. Last, we want to emphasize the controlled excitation $\tilde{G}^{\alpha_1\beta_2}_{\alpha_1\beta_0}$. Here, α_1 is the control but simultaneously part of the JW string $\mathcal{Z}^{\beta_1}_{\beta_0}$. Using all these properties allows us to implement $\exp(-i\delta t H_{\text{non-loc.}})$ with a total of 8 building blocks based on Figs. 3 and 8, as we depict in Fig. 5. Our circuit entails 26 MS gates whereas the implementation of each string separately (also using the symmetries and controlled rotations for the sake of comparability) amounts to 56, enabling a speedup of ~ 2.2. A naive implementation of each excitation separately without the use of symmetries gives rise to 176 MS gates, showcasing that the main benefit here stems from the symmetry exploitation rather than the parallelization.

Noise Modeling

So far, we have assumed ideal maximally entangling MS gates in our circuit decompositions. In practice on noisy quantum simulators, shorter circuits do not always guarantee results with higher fidelity. Our scenario is arguably more specific, given that we carry out the same types of gates on the same qubits as in ref. 24, just fewer times. Naively, one could estimate that we reduce the noise-strength for single,- and double excitations by factors of 2, and 4, respectively. Such simple scaling behavior holds, e.g. for depolarizing channels, but is not accurate for realistic noise models and experiments[77]. Therefore, the purpose of this section is to develop a realistic ion trap noise model, which we employ to assess if our reductions in MS gates actually result in higher fidelity building blocks for fermionic circuits.

We consider 12 $^{171}Yb^{+}$ ions trapped in a linear harmonic radio-frequency Paul trap[78], with axial trap frequency $\omega_z = 2\pi \times 0.5$ MHz and radial trap frequency $\omega_x = 2\pi \times 3.33$ MHz, such that the distances between adjacent ions lie in the range of 2.22 μm to 3.21 μm. We assume that each ion in the chain can be individually addressed with its own pair of red- and blue side-band Raman beams with optical frequencies $\omega_0 \pm \mu_i(t)$, where $\mu_i(t)$ is the time-dependent Raman detuning with respect to the spin resonance frequency $\omega_0 = 2\pi \times 12.643$ GHz[79] between the two spin-1/2 states which serve as the qubit computational basis states. We further assume that both Raman beams have equal time-dependent pulse amplitudes $\Omega^{(1)}_i(t) = \Omega^{(2)}_i(t)$ and originate from the same pulse-modulated laser source. Thus, AC stark shifts due to laser power fluctuations may be neglected as the contribution from the red and blue shifted Raman beams cancel each other out[80]. Under the rotating approximation $\omega_0 \gg \mu(t)$, and the Lamb-Dicke limit, the Hamiltonian of the experiment may be written as[80,81]

$$\begin{aligned} H_{\text{MS}}(t) \;=\; &\sum_i \sum_p \eta^{(i)}_p g^{(i)}(t)[a_p e^{-i\omega_p t} + a^{\dagger}_p e^{i\omega_p t}] \\ &\times[\cos(\phi)X_i + \sin(\phi)Y_i], \end{aligned} \tag{36}$$

where the indices i and p label the qubits/ions and radial motional modes, respectively. The Lamb-Dicke parameters $\eta^{(i)}_p \propto b^{(i)}_p/\sqrt{\omega_p}$ describe the coupling strength between qubit i and radial mode p and entail the normal mode transformation matrix $b^{(i)}_p$ of ion i and motional mode p with frequency ω_p, and a_p and $a^{\dagger}_p$ are the normal mode phonon creation- and annihilation operators. The $g^{(i)}(t) := \Omega^{(i)}(t)\sin(\int_0^t d\tau \mu^{(i)}(\tau))$ are the pulse functions defined through the aforementioned amplitudes and detunings. The phase ϕ is determined by the phase of the two Raman beams and is chosen such that either $\phi = 0$ for the **XX**-, or $\phi = \pi/2$ for the **YY**-interaction. The full experimental MS gate unitary corresponding to the Hamiltonian from equation (36) is described in the methods section.

For the modeling of different experimental error sources, we mostly follow ref. 82, which introduces a noise model for the global MS gate showing good agreement with experimental data. In particular, the authors consider vibrational mode frequency fluctuations $\omega_p \to \omega_p + \Delta\omega_p$, which lead to instabilities in both the geometric phases and displacements. Assuming thermal initial states of the vibrations[83], the decoherence from

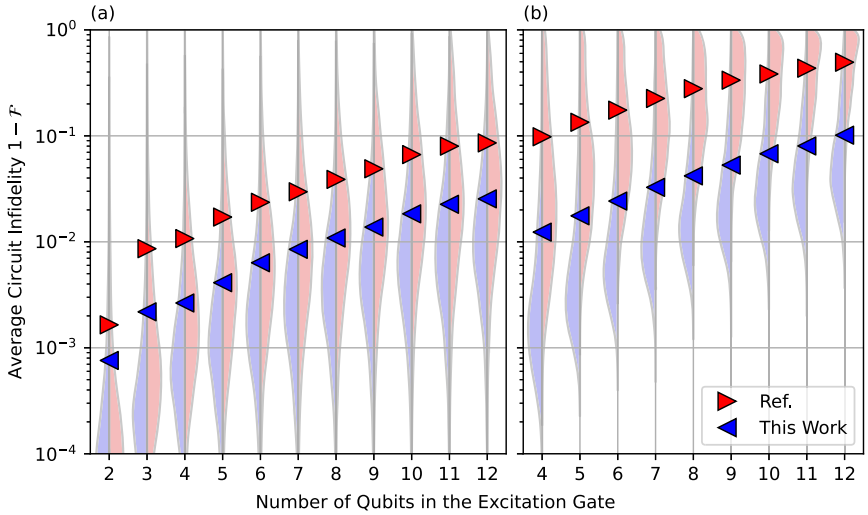

Fig. 6 | Benchmarks of the excitation-gate fidelities. Circuit infidelities for (**a**) single excitations, and (**b**) double excitations, for different number of qubits the gates act on, once with our decompositions (blue), and once with the one presented in ref. 24 (red). The statistics come from first sampling the frequency noise parameters paired with random excitation angles $M = 5000$ different times for each number of qubits. We then consider laser power fluctuations for each MS gate separately, thus resulting in averages over 10,000, and 20,000 experimental realizations of MS gates in our circuits for singles-, and doubles, respectively. Consequently, for the reference, we consider 20 000, and 80 000 realizations of MS gates. The markers show the mean of the respective distributions.

residual entanglement between electronic and vibrational states is further amplified. Laser power fluctuations of the two laser beams driving the MS interaction lead to fluctuations in the Rabi rates $\Omega^{(i)}(t) \to \Omega^{(i)}(t)(1 + \Delta\Omega^{(i)})$[81,82]. In addition, state preparation and measurement (SPAM) errors are considered. In their experiments, the authors find that vibrational frequency fluctuations and SPAM errors are the dominant sources of error. We focus on the former, given that scalable readout error mitigation methods exist[84], which could in principle handle the fundamental detection infidelity limit of $^{171}Yb^{+}$ ions which is about 10^{-3}[85]. We therefore consider a pulse modulation scheme which is robust against vibrational frequency fluctuations[81]. We provide a qualitative description in the methods section, whereas an in-depth guide is provided in Supplementary Note 7. For solving the optimization problem outlined in Sec. Pulse Modulation and Gate Stabilization, we use PyOptInferface[86,87] in combination with the Ipopt[88] software.

Assuming frequency fluctuations of 1 kHz[81] and power fluctuations of 0.5%, we find a two-qubit gate fidelity of $\mathcal{F}_2 = 99.97\%$, and observe an exponential decay in fidelity when increasing the number of qubits, up to a fidelity of $\mathcal{F}_{12} = 98.27\%$. We find that the decay is well described by $\mathcal{F}_2^{N(N-1)/2}$, which is motivated by the fact that an N-qubit MS gate implicitly entails $N(N-1)/2$ two-qubit MS gates. Another important feature is that the gate time of our optimized MS gates scales sub-linearly in the number of qubits, which conveniently yields sub-linear circuit times despite the linear locality of the JW mapping. A full characterization of the noise model is provided in Supplementary Note 8. More specifically, the assumed Lamb-Dicke parameters are shown in Supplementary Table 1, the optimized pulses are displayed in Supplementary Fig. 1, the gate fidelities as a function of the number of qubits are provided in Supplementary Fig. 2, and last the average laser power as a function of the number of qubits and gate time is analyzed in Supplementary Fig. 3.

Excitation Circuit Benchmarks

We first benchmark individual excitation gate decompositions, and, second, benchmark approximate ground state preparation of various molecules. We assume that single-qubit gate errors would be negligible and only apply noise to the MS gates according to the results section. We keep the frequency fluctuations $\Delta\omega_p$ fixed for every MS gate during one circuit execution, but assume different laser power fluctuations $\Delta\Omega^{(i)}$ for each MS gate within that circuit. This is motivated by the fact that the frequency fluctuations can be assumed constant on the timescale of minutes[81]. For all following simulations, we approximate the infinite sampling limit by computing expectation values based on statevector simulations for M noisy realizations of the circuits using Qiskit[89].

For benchmarking the individual excitation gates, we evaluate the average circuit infidelity $1 - \mathcal{F}$ with

$$\mathcal{F} = \frac{1}{2\pi}\int_{-\pi}^{\pi} d\theta |\langle\psi_{\mathrm{HF}}|U^{\dagger}(\theta)\widetilde{U}(\theta)|\psi_{\mathrm{HF}}\rangle|^2 , \tag{37}$$

for single and double excitations. Here, $\widetilde{U}(\theta)$ is a noisy excitation gate and $U(\theta)$ is an ideal excitation gate without noise. $|\psi_{\mathrm{HF}}\rangle$ is the state where the qubits p, for U_p^q, or p and q, for U_{pq}^{rs}, are in state $|1\rangle$ while all others are in state $|0\rangle$. We benchmark excitation gates that act on different number of qubits, from two to twelve, on arbitrary subsets of the linear ion trap. The results of our simulations are shown in Fig. 6. The statistics in Fig. 6 come from sampling the frequency noise parameters ($\Delta\omega_p$) $M = 5000$ different times for each locality, and then applying laser power fluctuations $\Delta\Omega^{(i)}$ to each MS gate separately. We see about half-an-order of magnitude improvements in the circuit infidelity for single excitations, when using our decomposition compared to the decomposition of ref. 24. For double excitations, this improvement increases to about one order of magnitude. These relative improvements are rather independent of the number of qubits the excitation gates act on, yet slowly decrease with increasing number of qubits. The stronger improvement for double excitations is naturally attributed to that fact that our decomposition reduces the number of MS gates by a factor of 4 instead of 2 for single excitations.

UCCSD Benchmarks

Further, we benchmark 11 molecules (H_2, HeH^+, $H3^+$, H_4, He_2, OH^-, HF, NeH^+, LiH, BeH_2, and H_2O), which geometries and electronic structure Hamiltonians are taken from the Pennylane dataset[90]. The Hartree-Fock ground state of diatomic He_2 has been calculated in the `6-31G` basis set, while for all other molecules, the basis set `STO-3G` was used. We apply the frozen core approximation to the molecules H_2O and BeH_2, in each case freezing two electrons associated to the spatial orbital with the lowest single-particle energy.

In order to apply our noise model, we first run a noiseless statevector calculation with the UCCSD ansatz optimized with ExcitationSolve[49] to find the optimal parameters for each molecule. We then build a new ansatz consisting of only excitations present in the UCCSD that have optimal parameter values with absolute values above a threshold of 10^{-2}. We note that in practice, one would pick the most important excitations either classically, e.g., based on second order Møller-Plesset perturbation theory (MP2) for double excitations[28], or on a quantum device using notions of ADAPT-VQE[91] specifically tailored for arbitrary excitations[49]. The combination of classical selection and warm-start strategies and adaptive quantum

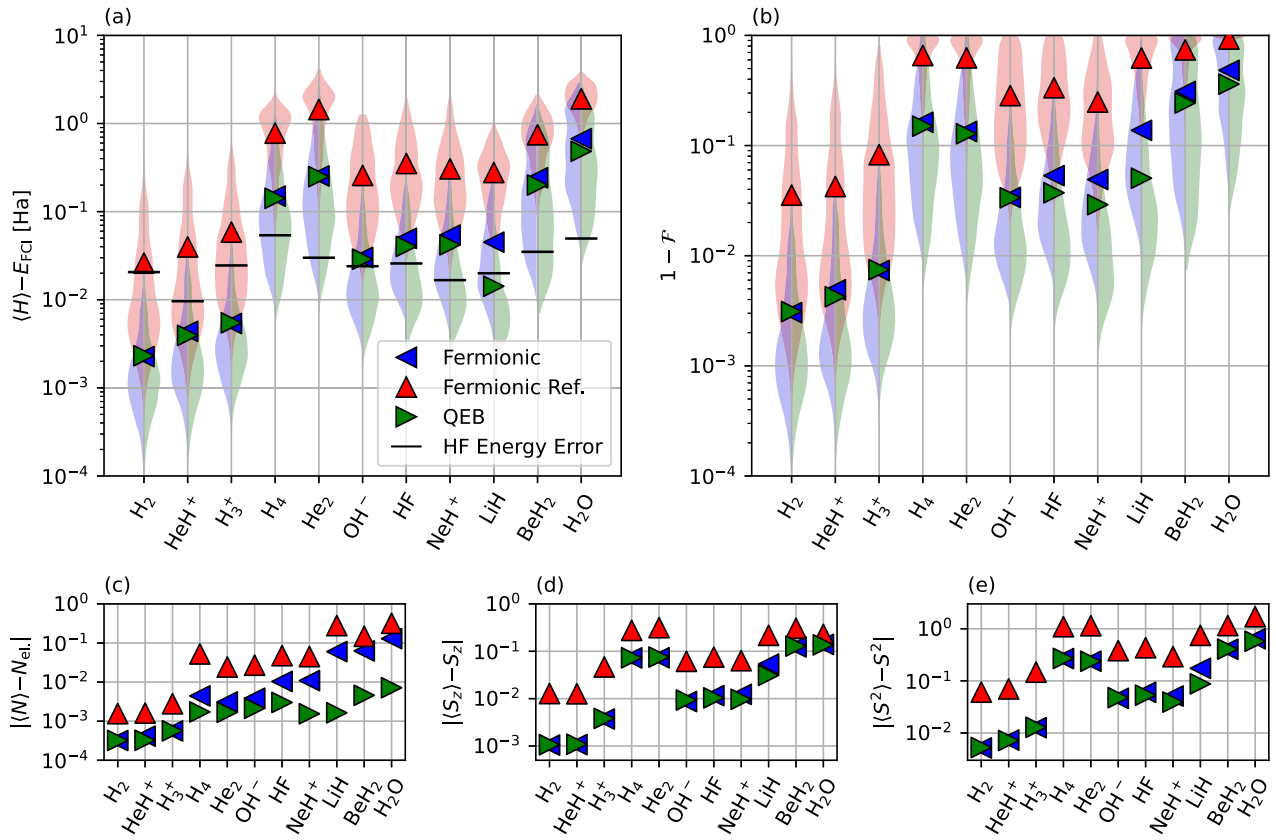

Fig. 7 | Benchmarks of UCCSD circuits for various molecules. Results from the molecular benchmarks. **a** Energy differences to the FCI result, (**b**) state infidelities w.r.t. to noiseless parameter-truncated states, (**c**) absolute errors in the particle number operator, (**d**) absolute errors in the S_z spin projection, and (**e**) absolute errors in the total spin S^2 for various molecules. The statistics are gathered by sampling the frequency noise parameters $M = 10\,000$ times for H_2, HeH^+, $H3^+$, then $M = 2500$ times for H_4, and $M = 1000$ times for He_2, OH^-, HF, NeH^+, LiH, BeH_2, and H_2O. Laser power fluctuations are then applied individually to each MS gate within each circuit execution. The markers show the mean of the respective distributions. We use our decompositions of fermionic excitations (blue) the decomposition from ref. 24 (red). In addition, we use our decomposition in combination with qubit excitations (green) instead of fermionic excitations. For H_2O and BeH_2 we use the frozen core approximation to reduce the needed qubits by two. The black horizontal lines show Hartree-Fock energy errors with respect to the FCI solution.

algorithms enables not only shallow circuits, but also significant speed-ups in convergence[92]. However, given that the goal of this section is to assess the quality of shallow UCCSD circuits under noise, the selection strategy to obtain the shallow circuit in the first place is secondary, and our brute-force selection based on a full UCCSD calculation is sufficient. The UCCSD ansatz is build once with fermionic excitations, and once with qubit excitations[55]. We use these parameter-truncated ansätze to perform our noisy simulations. We have verified that for both fermionic- and qubit excitations, the truncated ansätze can achieve chemical accuracy of 10^{-3} Ha[31] on an ideal device.

In Fig. 7 we present energy differences to the FCI result, state infidelities w.r.t. to noiseless parameter-truncated states, absolute errors in the particle number operator, absolute errors in the S_z spin projection, and absolute errors in the total spin S^2. This data is reported for the various molecules listed above. The statistics in Fig. 7 come from sampling the frequency noise parameters between $M = 10\,000$ for the smallest molecular systems, down to $M = 1000$ times for the largest molecules, and then applying laser power fluctuations to each MS gate within the UCCSD circuits. We perform our noisy simulations once with our decomposition of fermionic- and qubit excitations, and once with the decomposition presented in ref. 24.

In terms of energy error, we see consistent improvements between about half-an-order and one order of magnitude for all molecules when using our decomposition. For the state infidelities we outperform the decomposition of ref. 24 by up to one order of magnitude as well. Concerning the violation of conserved quantities, we also observe significant improvements for all tested molecules. All energy errors when using our fermionic decomposition, except for the molecules H_2, HeH^+, and $H3^+$, are still above the Hartree-Fock energy errors. This shows that the simulated noise significantly degrades the state even when only considering the most important excitations within our optimized circuit decompositions. This effect of the noise is less pronounced for the QEB circuits, where the energy error of the 12-qubit system LiH is below the Hartree-Fock error even under noise. In general, we observe mostly small but consistent improvements for qubit excitations over fermionic excitations across all larger systems. This is particularly pronounced on the electron number error which is consistently closer to zero, which we attribute to the QEB disturbing occupation numbers on less qubits in general. On the other hand, there is only little improvement for the spin projection error and total spin error when using QEB circuits, revealing that the occupation numbers within the individual spin-sectors are more prone to errors, which in the total electron number mostly cancel out. Overall, the advantage of using QEB circuits is less pronounced than on limited-connectivity hardware, since here the number of entangling gates and circuit depth remains identical, although the locality of the MS gates is reduced depending on the type of excitation. For the considered molecules, the list of important excitations is typically dominated by doubles acting on two spatial orbitals p, q, i.e., $G^{\alpha_q\beta_q}_{\alpha_p\beta_p}$, where fermionic- and qubit excitations turn out to be equivalent when the spin-orbitals are enumerated in alternating order (α_0, β_0, α_1, β_1, …). In fact, for H_2 and $H_3{}^+$, our fermionic- and QEB circuits are identical. The advantage of qubit excitations becomes most pronounced on the larger molecules HF, NeH^+, LiH, BeH_2, and H_2O, where long-range single-excitations and

doubles involving more than two spatial orbitals play significant roles. The largest benefit can be seen for LiH, which is due to the long-range fermionic double excitations $\alpha_1, \beta_1, \alpha_2, \beta_5$, and $\alpha_1, \beta_1, \beta_2, \alpha_5$, now acting on 4 instead of 10 and 8 qubits, respectively.

Overall, we conclude that our techniques provide significant improvements over the reference with respect to every metric. We also want to stress that our circuits could be readily paired with error mitigation techniques, likely leading accurate estimates of energy errors below the HF error. Since the focus of this work is on circuit decomposition techniques and the corresponding circuit quality improvements, we have deliberately refrained from using such techniques in order to isolate the influence of our methods.

Discussion

In this work, we introduced a parallelization scheme to reduce the number of MS gates for the implementation of fermionic excitations. Compared to previous works[24,25], we achieve a speedup of 2 and 4, for single- and double excitations, respectively. We further generalized our parallelization strategy to qubit single- and double excitations. We then studied our circuits in the presence of realistic experimental noise by emulating a 12-qubit linear ion trap at the pulse level, showcasing significant improvements over[24] across various molecular benchmarks, leading to fidelity improvements of up to one order of magnitude. We do however note that even with our improvements, meaningful accuracy improvements beyond HF theory would be tricky to achieve with the noise levels of current state-of-the-art quantum computers. Still, looking at the relative improvements in fidelity, our circuits hold the prospect of significantly improving fermionic simulations on real ion trap devices. And for near-term quantum hardware, pairing our technique with QEB ansätze is a promising avenue.

We note that our techniques could be readily extended to the simulation of fermion-boson interactions in a digital-analog fashion by encoding the bosonic operators into the vibrational modes of the ion chain[93], as it has been suggested in refs. 24,25. This gives access to systems such as the Fröhlich model[94], which captures the properties of polarons in some crystal structures[95,96]. Such simulations would extend the utility of our method beyond purely fermionic static- and dynamic properties to e.g., more complex phenomena in photochemistry[6,97,98], or the study of non-adiabatic electron-nuclear dynamics[74].

As we have pointed out, the parallelization techniques presented in this work are not readily applicable to other fermionic mappings. Meanwhile, the development of more efficient hardware-agnostic mappings is a flourishing field of ongoing research[12,18]. However, such mappings are typically developed with limited qubit connectivity in mind, and more importantly decompositions in terms of two-qubit gates. This raises the questions whether similar endeavors could lead to more efficient parallelizable mappings within the targeted MS gate set.

Last, we want to emphasize that our pulse simulations suggest that the MS gate time scales sub-linearly in the number of qubits, thus effectively achieving sub-linear circuit times even within linear-locality mapping such as JW, which ultimately highlights that trapped ions are promising platform for fermionic simulation.

Methods

The Backward MS Gate

One can entirely avoid Backward MS Gates by exploiting that MS Gates are equivalent to their "forward" counterparts[23]. Here, we assume an MS interaction acting on n qubits.

$$U_{\mathrm{MS}}(-\theta,\phi) = \begin{cases} U_{\mathrm{MS}}(\pi-\theta,\phi), & \text{for } n \text{ odd}, \\ U_{\mathrm{MS}}(\pi-\theta,\phi)\bigotimes_i \sigma_i(\phi), & \text{for } n \text{ even}. \end{cases} \tag{38}$$

For even n, this equivalence only holds up to local unitaries of the form $\sigma_i(\phi) := \cos(\phi)X_i + \sin(\phi)Y_i$. For the fully entangling MS gates **XX** and **YY** from equations (2) and (3), this boils down to a self-inverse property $U^\dagger = U$ up to local Paulis for an odd number of qubits. More preciseliy, we have

$$\mathbf{XX}^\dagger = \mathbf{XX}\begin{cases} \mathrm{I}, & \text{for n odd}, \\ \bigotimes_i \mathrm{X}_i, & \text{for n even}, \end{cases} \tag{39}$$

and

$$\mathbf{YY}^\dagger = \mathbf{YY}\begin{cases} \mathrm{I}, & \text{for n odd}, \\ \bigotimes_i \mathrm{Y}_i, & \text{for n even}. \end{cases} \tag{40}$$

The Jordan-Wigner Mapping

In order to emulate fermionic systems on a quantum computer, one needs a mapping between fermionic operators and qubit operators, i.e., a representation of fermionic operators in the Pauli basis. In this work, we focus on the Jordan-Wigner (JW) mapping. While often employed due to its inherent simplicity, the JW mapping faces the drawback of mapping fermionic operators on an n-mode system to terms with linear locality $\mathcal{O}(n)$. However, the linear locality of the JW mapping is to be seen as less problematic for ion trap quantum computers due to the all-to-all connectivity and native global interactions.

The fermionic (creation) annihilation operators $a^{(\dagger)}$ satisfy the canonical commutation relations $\{a_p, a_q^\dagger\} = \delta_{pq}$ and $\{a_p, a_q\} = \{a_p^\dagger, a_q^\dagger\} = 0$. Under the JW mapping, these fermionic operators take the following form:

$$a_p^{(\dagger)} \to \frac{1}{2}\left(\bigotimes_{k<p} Z_k\right) \otimes (X_p \mp i Y_p). \tag{41}$$

Note that the non-locality arises from the $\mathcal{O}(n)$-local parity strings consisting of Pauli-Z operators, which ensure the proper anticommutation relations. Through the course of this work, we use the MS gate to efficiently take these contributions into account.

Circuits for Controlled Single Excitations

When considering the JW-mapped expression for the controlled single excitation

$$G_{pj}^{qj} \to -\frac{1}{4}(I_j - Z_j)\mathcal{Z}_p^q(Y_pX_q - X_pY_q), \tag{42}$$

where we again assumed $p < q$, we must distinguish between two cases.

Case 1: If $j < p$ or $j > q$, the control qubit j is not affected by the single-excitation generator G_p^q. Therefore, we can simply obtain the circuit by replacing the $R_z(\theta)$ gates in Fig. 2 by controlled Z-rotations $\mathrm{C}_j R_z(-\theta)$, as depicted in Fig. 8. Alternatively, one may implement G_p^q and $Z_jG_p^q$ separately. The latter can be achieved by adding j to the MS interaction.

Case 2: If $p < j < q$, equation (42) contains the expression $-(I_j - Z_j)Z_j = I_j - Z_j$. When using controlled rotations, this effectively removes qubit j from the MS interaction in Fig. 2 and turns it into a control qubit (Fig. 8a). Optionally, the separate decomposition of G_p^q and $Z_jG_p^q$ also works, though now the latter term is achieved by removing j from the MS interaction.

Compared to the technique from ref. 24, our circuits once again cut the number of MS gates by half as for the regular single excitations.

Simulation with Real-Valued Orbitals

For real orbitals, the one- and two-electron terms are real, thus simplifying the symmetries to $h_{pq} = h_{qp}$ and $h_{pqrs} = h_{qpsr} = h_{rspq} = h_{srqp}$. This changes the electronic Hamiltonian to

$$H_{el.} = \frac{1}{2}\sum_{pq} h_{pq}\widetilde{G}_p^q + \frac{1}{4}\sum_{pqrs} h_{pqrs}\widetilde{G}_{pq}^{rs}, \tag{43}$$

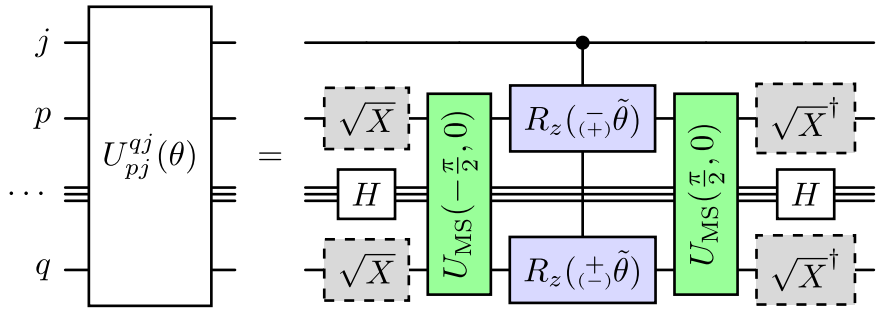

Fig. 8 | Circuit decomposition of the controlled single-excitation gate. Circuit decomposition of the controlled single-excitation gate $U_{pj}^{qj}(\theta) = \exp(-i\theta G_{pj}^{qj})$ using the **XX** gate in terms of two MS gates and two $\mathrm{C}_j R_z$ gates. The dots ⋯ labeling the quantum wire bundle represent all qubits affected by the parity string $\mathcal{Z}_p^q$, except j if $p < j < q$. The light-gray dashed gates are used if the number of qubits in the wire bundle is odd. The signs in brackets account for the sign flip for $p < j < q$.

thus removing all the antisymmetric terms from equation (15). At the same time, real orbitals introduce four additional permutation symmetries to the two-electron integrals, namely $h_{pqrs} = h_{rqps} = h_{spqr} = h_{psrq} = h_{qrsp}$[50]. This allows as to further simplify the Hamiltonian to

$$H_{\mathrm{el.}} = \frac{1}{2}\sum_{pq} h_{pq}\widetilde{G}_p^q + \frac{1}{8}\sum_{pqrs} h_{pqrs}(\widetilde{G}_{pq}^{rs} + \widetilde{G}_{ps}^{rq}). \tag{44}$$

A derivation is provided in Supplementary Note 6. The term $\widetilde{G}_{pq}^{rs} + \widetilde{G}_{ps}^{rq}$ boils down to 4 Pauli strings instead of 8, which we can use to simplify the circuit structure. We use the antisymmetrized version $G_{pq}^{rs} + G_{ps}^{rq}$ to derive the corresponding circuit. From equation (24), we conclude that

$$\begin{aligned} &G_{pq}^{rs} + G_{ps}^{rq} \to \tfrac{1}{4}\mathcal{Z}_{pq}^{rs} \\ &\times (X_pX_qX_rY_s - X_pY_qX_rX_s + Y_pX_qY_rY_s - Y_pY_qY_rX_s). \end{aligned} \tag{45}$$

We can implement this term using the circuit from Fig. 3 by removing the R_z gates on qubits q_p and q_r and adjusting the angles of the R_z gates on qubits q_q and q_s. Despite the reduction in Pauli strings, it still requires 4 MS gates. Hence, the four additional symmetries do not benefit the runtime of our quantum simulation scheme. However, assuming that $h_{pqrs} \neq h_{prsq} \neq 0$, the full 8 strings will be restored. Nonetheless, the use of real orbitals halves the number of terms in the Hamiltonian and followingly the depth of the Trotter step circuit. On a side note, linear combinations of the type $G_{pq}^{rs} \pm G_{ps}^{rq}$, also referred to as coupled exchange operators, have recently proven to be useful in variations of UCCSD theory[99].

The Experimental MS Gate

In the following, we focus on the **XX** gate with $\phi = 0$ to simplify the notation. All considerations hold equivalently for the **YY** gate. The unitary operator corresponding to the experimental MS gate is obtained exactly by solving the time evolution operator via second-order Magnus expansion[82,100], and reads

$$\begin{aligned} U_{\mathrm{MS}}(t) = &\exp\left(-i\sum_{i<j}^{N}\chi^{(i,j)}(t)X_iX_j\right) \\ &\times \exp\left(\sum_{i}^{N}\sum_{p}^{N}[\alpha_p^{(i)}(t)a_p^\dagger - \mathrm{H.c.}]X_i\right). \end{aligned} \tag{46}$$

The first part implements the spin-spin interaction between the ions electronic states/logical qubit states, whereas the second part captures the spin-displacement coupling between the electronic states and vibrational mode coherent states. Note that for $\chi^{(i,j)} = \theta/2$, the first term corresponds to the ideal MS gate assumed in equation (1). The geometric phases defining the Ising evolution are given by

$$\begin{aligned} \chi^{(i,j)}(t) = &\sum_p \eta_p^{(i)}\eta_p^{(j)}\int_0^t d\tau_2\int_0^{\tau_2} d\tau_1 g^{(i)}(\tau_1)g^{(j)}(\tau_2) \\ &\times \sin(\omega_p(\tau_2 - \tau_1)), \end{aligned} \tag{47}$$

and the phase space displacements of the vibrational modes are

$$\alpha_p^{(i)}(t) = \int_0^t d\tau g^{(i)}(\tau)e^{i\omega_p\tau}. \tag{48}$$

By tracing out the phonon modes, one can quantify the decoherence from residual ion-vibration entanglement[82] and obtain the quantum channel acting solely on the qubit states.

Pulse Modulation and Gate Stabilization

In the following, we briefly recap the power-optimal stabilized entangling gate scheme from ref. 81. A more detailed elaboration is provided in Supplementary Note 7. The pulse functions (which entail both the amplitude and detuning) are expanded in a Fourier-sine basis. The pulse acting on the i^{th} ion is defined as

$$g^{(i)}(t) = \sum_{n=1}^{N_A} A_n^{(i)} \sin\left(2\pi n\frac{t}{T}\right) \tag{49}$$

where T is the gate time, $A_n^{(i)}$ the n^{th} Fourier coefficient and N_A the total amount of Fourier coefficients. By construction, the pulse vanishes at $t = 0$ and $t = T$. To ensure experimental viability of the pulses, the highest Fourier frequency is restricted to $\omega_{N_A} = 2\pi \times N_A/T \leq 2\pi \times 5\,MHz$, which is well within the capabilities of acusto-optical or electro-optical modulators typically used to modulate the laser beams. To avoid residual ion-vibration entanglement, the pulses must satisfy the property $\alpha_p^{(i)}(T) = 0$, which translates into N linear constraints of the type $\sum_{n=1}^{N_A} M_{pn}A_n^{(i)} = 0$ with $M_{pn} = \int_0^t d\tau \sin(2\pi n\tau/T)e^{i\omega_p\tau}$. To additionally stabilize this condition against vibrational mode fluctuations $\Delta\omega_p$ up to order S, the conditions $\partial^s/\partial\omega_p^s\,\alpha_p^{(i)}(T) = 0$ must be satisfied, which translates into $N \times S$ additional linear constraints $\sum_{n=1}^{N_A} M_{pn}^{(s)}A_n^{(i)} = 0$. By computing an orthonormal basis of the nullspace of M, one restricts the pulse-space basis to only such solutions which ensure vanishing residual ion-vibration entanglement, and reduces the dimension of our optimization problem. This then conveniently removes the second term of equation (46). In our simulations, we use $S = 10$ as we find that the dimension of the nullspace does not decrease beyond that.

Next, we require that all pair-wise entanglement degrees satisfy $\chi^{(i,j)}(T) = \pi/4$ for qubits i and j participating in the maximally entangling MS interaction. For a global MS interaction, this translates into $N \times (N-1)/2$ quadratic constraints of the type $\sum_{n,m=1}^{N_A} A_n^{(i)}S_{nm}A_m^{(j)} = \pi/4$ (cf. Supplementary Note 7). To make the entanglement degree robust against motional frequency fluctuations, one can again enforce vanishing derivatives up to some order K, which then yields $K \times N \times (N-1)/2$ additional quadratic constraints of the type $\sum_{n,m=1}^{N_A} A_n^{(i)}S_{nm}^{(k)}A_j^{(m)} = 0$. According to ref. 81, the average laser power grows exponentially in K, which is why we choose the lowest stabilization order $K = 1$ in our simulations.

The objective of finding power-optimal stabilized gates then boils down to minimizing the average laser power per ion $\gamma^2 := 1/N\sum_i\sum_n(A_n^{(i)})^2$ under the quadratic constraints, which belongs to a class of optimization problems referred to as quadratically constrained quadratic program (QCQP)[101]. For experimental application, optimizing the maximum instead of the average power would be more relevent. However,[43] show that both objectives lead to similar pulse shapes, with optimization on average power being more numerically stable. For two-qubit MS gates, the globally optimal solution can be efficiently constructed[43,81]. While the procedure does not generalize to global MS gates, it serves as a valuable initialization strategy in our simulations.

Data availability

The datasets generated and/or analysed during the current study are available in the Zenodo repository, https://doi.org/10.5281/zenodo.18789051[103].

Code availability

The underlying code for this study is available in GitHub and can be accessed via this link https://github.com/dlr-wf/MS-gate-noise-model.

Received: 14 April 2025; Accepted: 12 March 2026;
Published online: 27 March 2026

References

1. Kandala, A. et al. Hardware-efficient variational quantum eigensolver for small molecules and quantum magnets. *nature* **549**, 242–246 (2017).
2. O'Malley, P. J. J. et al. Scalable quantum simulation of molecular energies. *Phys. Rev. X* **6**, 031007 (2016).
3. McArdle, S., Endo, S., Aspuru-Guzik, A., Benjamin, S. C. & Yuan, X. Quantum computational chemistry. *Rev. Mod. Phys.* **92**, 015003 (2020).
4. Liu, H. et al. Prospects of quantum computing for molecular sciences. *Mater. Theory* **6**, 11 (2022).
5. Magann, A. B., Grace, M. D., Rabitz, H. A. & Sarovar, M. Digital quantum simulation of molecular dynamics and control. *Phys. Rev. Res.* **3**, 023165 (2021).
6. Ollitrault, P. J., Miessen, A. & Tavernelli, I. Molecular quantum dynamics: A quantum computing perspective. *Acc. Chem. Res.* **54**, 4229–4238 (2021).
7. Clinton, L. et al. Towards near-term quantum simulation of materials. *Nat. Commun.* **15**, 211 (2024).
8. Wang, P.-H., Chen, J.-H., Yang, Y.-Y., Lee, C. & Tseng, Y. J. Recent advances in quantum computing for drug discovery and development. *IEEE Nanotechnol. Mag.* **17**, 26–30 (2023).
9. Jordan, P. & Wigner, E. P.*Über das paulische äquivalenzverbot* (Springer, 1993).
10. Bravyi, S. B. & Kitaev, A. Y. Fermionic quantum computation. *Ann. Phys.* **298**, 210–226 (2002).
11. Seeley, J. T., Richard, M. J. & Love, P. J. The Bravyi-Kitaev transformation for quantum computation of electronic structure. *J.Chem. Phys.* **137**, (2012).
12. Miller, A., Zimborás, Z., Knecht, S., Maniscalco, S. & García-Pérez, G. Bonsai algorithm: Grow your own fermion-to-qubit mappings. *PRX Quantum* **4**, 030314 (2023).
13. Chiew, M. & Strelchuk, S. Discovering optimal fermion-qubit mappings through algorithmic enumeration. *Quantum* **7**, 1145 (2023).
14. Setia, K. & Whitfield, J. D. Bravyi-kitaev superfast simulation of electronic structure on a quantum computer. *J. Chem. Phys.* **148**, (2018).
15. Steudtner, M. & Wehner, S. Fermion-to-qubit mappings with varying resource requirements for quantum simulation. *N. J. Phys.* **20**, 063010 (2018).
16. Havlíček, V. cv, Troyer, M. & Whitfield, J. D. Operator locality in the quantum simulation of fermionic models. *Phys. Rev. A* **95**, 032332 (2017).
17. Steudtner, M. & Wehner, S. Quantum codes for quantum simulation of fermions on a square lattice of qubits. *Phys. Rev. A* **99**, 022308 (2019).
18. Miller, A., Glos, A. & Zimbor s, Z. Treespilation: architecture- and state-optimised fermion-to-qubit mappings. *npj Quantum Inf.* **12**, 6 (2026).
19. Benhelm, J., Kirchmair, G., Roos, C. F. & Blatt, R. Towards fault-tolerant quantum computing with trapped ions. *Nat. Phys.* **4**, 463–466 (2008).
20. Taylor, R. L. et al. A study on fast gates for large-scale quantum simulation with trapped ions. *Sci. Rep.* **7**, 46197 (2017).
21. Sørensen, A. & Mølmer, K. Quantum computation with ions in thermal motion. *Phys. Rev. Lett.* **82**, 1971 (1999).
22. Sørensen, A. & Mølmer, K. Entanglement and quantum computation with ions in thermal motion. *Phys. Rev. A* **62**, 022311 (2000).
23. Müller, M., Hammerer, K., Zhou, Y. L., Roos, C. F. & Zoller, P. Simulating open quantum systems: from many-body interactions to stabilizer pumping. *N. J. Phys.* **13**, 085007 (2011).
24. Casanova, J., Mezzacapo, A., Lamata, L. & Solano, E. Quantum simulation of interacting fermion lattice models in trapped ions. *Phys. Rev. Lett.* **108**, 190502 (2012).
25. Lamata, L., Mezzacapo, A., Casanova, J. & Solano, E. Efficient quantum simulation of fermionic and bosonic models in trapped ions. *EPJ Quantum Technol.* **1**, 1–13 (2014).
26. Martinez, E. A. et al. Real-time dynamics of lattice gauge theories with a few-qubit quantum computer. *Nature* **534**, 516–519 (2016).
27. Hempel, C. et al. Quantum chemistry calculations on a trapped-ion quantum simulator. *Phys. Rev. X* **8**, 031022 (2018).
28. Romero, J. et al. Strategies for quantum computing molecular energies using the unitary coupled cluster ansatz. *Quantum Sci. Technol.* **4**, 014008 (2018).
29. Shen, Y. et al. Quantum implementation of the unitary coupled cluster for simulating molecular electronic structure. *Phys. Rev. A* **95**, 020501 (2017).
30. Bartlett, R. J., Kucharski, S. A. & Noga, J. Alternative coupled-cluster ansätze ii. the unitary coupled-cluster method. *Chem. Phys. Lett.* **155**, 133–140 (1989).
31. Peruzzo, A. et al. A variational eigenvalue solver on a photonic quantum processor. *Nat. Commun.* **5**, 4213 (2014).
32. Anand, A. et al. A quantum computing view on unitary coupled cluster theory. *Chem. Soc. Rev.* **51**, 1659–1684 (2022).
33. Maslov, D. & Nam, Y. Use of global interactions in efficient quantum circuit constructions. *N. J. Phys.* **20**, 033018 (2018).
34. van de Wetering, J. Constructing quantum circuits with global gates. *N. J. Phys.* **23**, 043015 (2021).
35. Ivanov, S. S., Ivanov, P. A. & Vitanov, N. V. Efficient construction of three- and four-qubit quantum gates by global entangling gates. *Phys. Rev. A* **91**, 032311 (2015).
36. Groenland, K., Witteveen, F., Schoutens, K. & Gerritsma, R. Signal processing techniques for efficient compilation of controlled rotations in trapped ions. *N. J. Phys.* **22**, 063006 (2020).
37. Berry, D. W., Childs, A. M., Su, Y., Wang, X. & Wiebe, N. Time-dependent hamiltonian simulation with l^1-norm scaling. *Quantum* **4**, 254 (2020).
38. Lee, C.-K., Hsieh, C.-Y., Zhang, S. & Shi, L. Variational quantum simulation of chemical dynamics with quantum computers. *J. Chem. Theory Comput.* **18**, 2105–2113 (2022).
39. Bultrini, D. & Vendrell, O. Mixed quantum-classical dynamics for near term quantum computers. *Nat., Commun. Phys.* **6**, 328 (2023).
40. Martinez, E. A., Monz, T., Nigg, D., Schindler, P. & Blatt, R. Compiling quantum algorithms for architectures with multi-qubit gates. *N. J. Phys.* **18**, 063029 (2016).

41. Debnath, S. et al. Demonstration of a small programmable quantum computer with atomic qubits. *Nature* **536**, 63–66 (2016).
42. Figgatt, C. et al. Parallel entangling operations on a universal ion-trap quantum computer. *Nature* **572**, 368–372 (2019).
43. Grzesiak, N. et al. Efficient arbitrary simultaneously entangling gates on a trapped-ion quantum computer. *Nat. Commun.* **11**, 2963 (2020).
44. Nebendahl, V., Häffner, H. & Roos, C. F. Optimal control of entangling operations for trapped-ion quantum computing. *Phys. Rev. A* **79**, 012312 (2009).
45. Gard, B. T. et al. Efficient symmetry-preserving state preparation circuits for the variational quantum eigensolver algorithm. *npj Quantum Inf.* **6**, 10 (2020).
46. Trotter, H. F. On the product of semi-groups of operators. *Proc. Am. Math. Soc.* **10**, 545–551 (1959).
47. Suzuki, M. Generalized trotter's formula and systematic approximants of exponential operators and inner derivations with applications to many-body problems. *Commun. Math. Phys.* **51**, 183–190 (1976).
48. Kottmann, J. S., Anand, A. & Aspuru-Guzik, A. A feasible approach for automatically differentiable unitary coupled-cluster on quantum computers. *Chem. Sci.* **12**, 3497–3508 (2021).
49. Jäger, J. et al. Fast gradient-free optimization of excitations in variational quantum eigensolvers. *Commun. Phys.* **8**. https://doi.org/10.1038/s42005-025-02375-9(2025).
50. Szabo, A. & Ostlund, N. S.*Modern quantum chemistry: introduction to advanced electronic structure theory* (Dover Publications, 1996), 1st edn.
51. Kornell, A. & Selinger, P. Some improvements to product formula circuits for hamiltonian simulation. arXiv preprint (2023).
52. Lee, J., Huggins, W. J., Head-Gordon, M. & Whaley, K. B. Generalized unitary coupled cluster wave functions for quantum computation. *J. Chem. theory Comput.* **15**, 311–324 (2018).
53. Arrazola, J. M. et al. Universal quantum circuits for quantum chemistry. *Quantum* **6**, 742 (2022).
54. Haidar, M., Rancic, M. J., Maday, Y. & Piquemal, J.-P. Extension of the trotterized unitary coupled cluster to triple excitations. *J. Phys. Chem. A* **127**, 3543–3550 (2023).
55. Yordanov, Yordan S. et al. Qubit-excitationbased adaptive variational quantum eigensolver. *Commun. Phys.* **4**. https://doi.org/10.1038/s42005-021-00730-0 (2021).
56. Marx, D. & Hutter, J. Ab Initio Molecular Dynamics. *Apr*. https://doi.org/10.1017/cbo9780511609633 (2009).
57. Richings, G. W. et al. Quantum dynamics simulations using Gaussian wavepackets: the vMCG method. *Int. Rev. Phys. Chem.* **34**, 269–308 (2015).
58. Hansson, T., Oostenbrink, C. & van Gunsteren, W. Molecular dynamics simulations. *Curr. Opin. Struct. Biol.* **12**, 190–196 (2002).
59. Iftimie, R., Minary, P. & Tuckerman, M. E. Ab initio molecular dynamics: Concepts, recent developments, and future trends. *Proc. Natl. Acad. Sci.* **102**, 6654–6659 (2005).
60. He, X., Zhu, Y., Epstein, A. & Mo, Y. Statistical variances of diffusional properties from ab initio molecular dynamics simulations. *npj Comput. Mater* **4**, 18 (2018).
61. Mosconi, E., Azpiroz, J. M. & De Angelis, F. Ab initio molecular dynamics simulations of methylammonium lead iodide perovskite degradation by water. *Chem. Mater.* **27**, 4885–4892 (2015).
62. Thomas, M., Brehm, M., Fligg, R., Vöhringer, P. & Kirchner, B. Computing vibrational spectra from ab initio molecular dynamics. *Phys. Chem. Chem. Phys.* **15**, 6608 (2013).
63. Crespo-Otero, R. & Barbatti, M. Recent advances and perspectives on nonadiabatic mixed quantum–classical dynamics. *Chem. Rev.* **118**, 7026–7068 (2018).
64. Wang, Y., Liu, X., Cui, G., Fang, W. & Thiel, W. Photoisomerization of arylazopyrazole photoswitches: Stereospecific excited-state relaxation. *Angew. Chem.* **128**, 14215–14219 (2016).
65. Curchod, B. F. E. & Orr-Ewing, A. J. Perspective on theoretical and experimental advances in atmospheric photochemistry. *J. Phys. Chem. A* **128**, 6613–6635 (2024).
66. Hernández, F. J. & Crespo-Otero, R. Modeling excited states of molecular organic aggregates for optoelectronics. *Annu. Rev. Phys. Chem.* **74**, 547–571 (2023).
67. Nelson, T. R. et al. Non-adiabatic excited-state molecular dynamics: Theory and applications for modeling photophysics in extended molecular materials. *Chem. Rev.* **120**, 2215–2287 (2020).
68. Nelson, T. et al. Ultrafast photodissociation dynamics of nitromethane. *J. Phys. Chem. A* **120**, 519–526 (2016).
69. Wong, B. M. & Lee, J. W. Anomalous optoelectronic properties of chiral carbon nanorings… and one ring to rule them all. *J. Phys. Chem. Lett.* **2**, 2702–2706 (2011).
70. Fidler, A. F., Singh, V. P., Long, P. D., Dahlberg, P. D. & Engel, G. S. Dynamic localization of electronic excitation in photosynthetic complexes revealed with chiral two-dimensional spectroscopy. *Nat. Commun* **5**, 3286 (2014).
71. Fernandez-Alberti, S., Kleiman, V. D., Tretiak, S. & Roitberg, A. E. Nonadiabatic molecular dynamics simulations of the energy transfer between building blocks in a phenylene ethynylene dendrimer. *J. Phys. Chem. A* **113**, 7535–7542 (2009).
72. Nelson, T., Fernandez-Alberti, S., Roitberg, A. E. & Tretiak, S. Electronic delocalization, vibrational dynamics, and energy transfer in organic chromophores. *J. Phys. Chem. Lett.* **8**, 3020–3031 (2017).
73. Olaya-Agudelo, Vanessa C. et al. Simulating open-system molecular dynamics on analog quantum computers **7**, https://doi.org/10.1103/physrevresearch.7.023215(2025).
74. Ha, Jong-Kwon & MacDonell, Ryan J. Analog quantum simulation of coupled electron-nuclear dynamics in molecules. *Chem. Sci*. https://doi.org/10.1039/d5sc04076k(2025).
75. Sun, Q. et al. Pyscf: the Python-based simulations of chemistry framework. *Wiley Interdiscip. Rev.: Computational Mol. Sci.* **8**, e1340 (2018).
76. Sun, Q. et al. Recent developments in the pyscf program package. *The J. Chem. Phys.* **153**, (2020).
77. Koenig, K. F., Reinecke, F., Hahn, W. & Wellens, T. Inverted-circuit zero-noise extrapolation for quantum-gate error mitigation. *Phys. Rev. A* **110**, 042625 (2024).
78. Deslauriers, L. et al. Zero-point cooling and low heating of trapped $^{111}Cd^{+}$ ions. *Phys. Rev. A* **70**, 043408 (2004).
79. Olmschenk, S. et al. Manipulation and detection of a trapped yb^{+} hyperfine qubit. *Phys. Rev. A* **76**, 052314 (2007).
80. Morong, W. et al. Engineering dynamically decoupled quantum simulations with trapped ions. *PRX Quantum* **4**, 010334 (2023).
81. Blümel, R. et al. Power-optimal, stabilized entangling gate between trapped-ion qubits. npj Quantum Information 7 (2021). https://doi.org/10.1038/s41534-021-00489-w.
82. Lotshaw, P. C. et al. Modeling noise in global mølmer-sørensen interactions applied to quantum approximate optimization. *Phys. Rev. A* **107**, 062406 (2023).
83. Roos, C. F. Ion trap quantum gates with amplitude-modulated laser beams. *N. J. Phys.* **10**, 013002 (2008).
84. Nation, P. D., Kang, H., Sundaresan, N. & Gambetta, J. M. Scalable mitigation of measurement errors on quantum computers. *PRX Quantum* **2**, 040326 (2021).
85. Noek, R. et al. High speed, high fidelity detection of an atomic hyperfine qubit. *Opt. Lett.* **38**, 4735–4738 (2013).
86. Yang, Y. et al. PyOptInterface: Design and implementation of an efficient modeling language for mathematical optimization. https://doi.org/10.48550/ARXIV.2405.10130(2024).
87. Yang, Y. et al. Accelerating Optimal Power Flow With Structure-Aware Automatic Differentiation and Code Generation. *IEEE Trans. Power Syst.* **40**, 1172–1175 (2025).

88. Wächter, A. & Biegler, L. T. On the implementation of an interior-point filter linesearch algorithm for large-scale nonlinear programming. Mathematical Programming 106, 25-57 (2005).
89. Javadi-Abhari, Ali et al. Quantum computing with Qiskit. arXiv (2024). https://doi.org/10.48550/ARXIV.2405.08810.
90. Azad, U. & Fomichev, S. Pennylane quantum chemistry datasets. https://pennylane.ai/datasets/he2-molecule (2023).
91. Grimsley, Harper R. et al. An adaptive variational algorithm for exact molecular simulations on a quantum computer. *Nat. Commun.* **10**. https://doi.org/10.1038/s41467-019-10988-2(2019).
92. Haas, M., Kaldenbach, T. N., Hammerschmidt, T. & Barragan-Yani, D. Efficient operator selection and warm-start strategy for excitations in variational quantum eigensolvers. arXiv preprint (2026).
93. Leibfried, D., Blatt, R., Monroe, C. & Wineland, D. Quantum dynamics of single trapped ions. *Rev. Mod. Phys.* **75**, 281–324 (2003).
94. Mahan, G. D.*Many-particle physics* (Springer Science & Business Media, 2013).
95. Franchini, C., Reticcioli, M., Setvin, M. & Diebold, U. Polarons in materials. *Nat. Rev. Mater.* **6**, 560–586 (2021).
96. Aihemaiti, N., Li, Z. & Peng, S. Perspective on high-resolution characterizations of polarons in halide perovskites. *Chem. Mater.* **36**, 5297–5312 (2024).
97. Bauer, B., Bravyi, S., Motta, M. & Chan, G. K.-L. Quantum algorithms for quantum chemistry and quantum materials science. *Chem. Rev.* **120**, 12685–12717 (2020).
98. Ollitrault, P. J., Mazzola, G. & Tavernelli, I. Nonadiabatic molecular quantum dynamics with quantum computers. *Phys. Rev. Lett.* **125**, 260511 (2020).
99. Ramôa, M., Anastasiou, P.G., Santos, L.P. et al. Reducing the resources required by ADAPT-VQE using coupled exchange operators and improved subroutines. *npj Quantum Inf.* **11**, 86 (2025)
100. Zhu, S.-L., Monroe, C. & Duan, L.-M. Arbitrary-speed quantum gates within large ion crystals through minimum control of laser beams. *Europhys. Lett.* **73**, 485 (2006).
101. Boyd, S. & Vandenberghe, L.*Convex optimization* (Cambridge University Press, 2004).
102. Kay, A. Tutorial on the quantikz package. arXiv preprint (2018).
103. Kaldenbach, Thierry N. et al. Improved Strategies for Fermionic Quantum Simulation with Global Interactions - Data. (2026). https://doi.org/10.5281/zenodo.18789051.

Acknowledgements

This project was funded by the DLR Quantum Computing Initiative and the Federal Ministry for Economic Affairs and Climate Action; https://qci.dlr.de/quanticom(T.N.K, E.S, G.B.). We thank Max Haas for helpful comments on the manuscript. All quantum circuits were drawn using the LaTeX-package `Quantikz`[102].

Author contributions

T.N.K. developed the theoretical formalism, the simulation code, and performed the noisy simulations. T.N.K. and N.S. conceived the noise model. E.S. enabled the HPC integration of the simulation code. G.B. worked out the practical use cases in quantum chemistry and material science. T.N.K. led the effort in writing the manuscript.

Funding

Open Access funding enabled and organized by Projekt DEAL.

Competing interests

A patent application filed by the German Aerospace Center (Deutsches Zentrum für Luft- und Raumfahrt e.V., DLR), currently pending with the German Patent and Trade Mark Office (Deutsches Patent- und Markenamt, DPMA), covers aspects of this work. It specifically includes the presented quantum circuits for symmetrized and antisymmetrized single-, controlled single-, and double-excitation operators and their applicability to UCCSD calculations and Hamiltonian simulation. The listed inventors are Thierry N. Kaldenbach, Gabriel Breuil, and Eric Breitbarth. The application number is DE 10 2025 133 101.4, with the German title “Quantenschaltkreis". The authors declare no other financial or non-financial competing interests.

Additional information

Supplementary information The online version contains supplementary material available at https://doi.org/10.1038/s41534-026-01223-0.

Correspondence and requests for materials should be addressed to Thierry N. Kaldenbach.